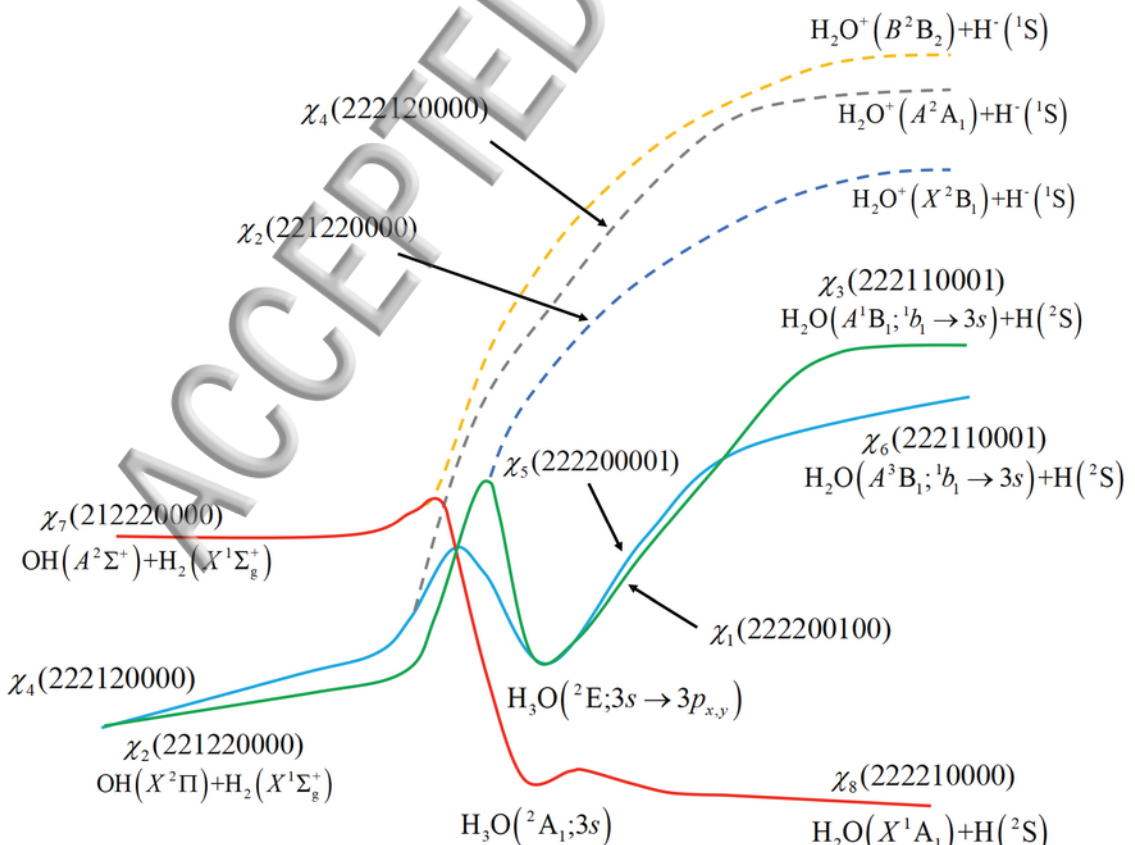
$H_2O^+(B^2B_2)+H^-(^1S)$
$H_2O^+(A^2A_1)+H^-(^1S)$
$H_2O^+(X^2B_1)+H^-(^1S)$
$\chi_4(222120000)$
$\chi_2(221220000)$
$\chi_3(222110001)$
$H_2O(A^1B_1;{}^1b_1\rightarrow 3s)+H(^2S)$
$\chi_6(222110001)$
$H_2O(A^3B_1;{}^1b_1\rightarrow 3s)+H(^2S)$
$\chi_5(222200001)$
$\chi_7(212220000)$
$OH(A^2\Sigma^+)+H_2(X^1\Sigma_g^+)$
$\chi_1(222200100)$
$\chi_4(222120000)$
$H_3O(^2E;3s\rightarrow 3p_{x,y})$
$\chi_2(221220000)$
$OH(X^2\Pi)+H_2(X^1\Sigma_g^+)$
$\chi_8(222210000)$
$H_3O(^2A_1;3s)$
$H_2O(X^1A_1)+H(^2S)$

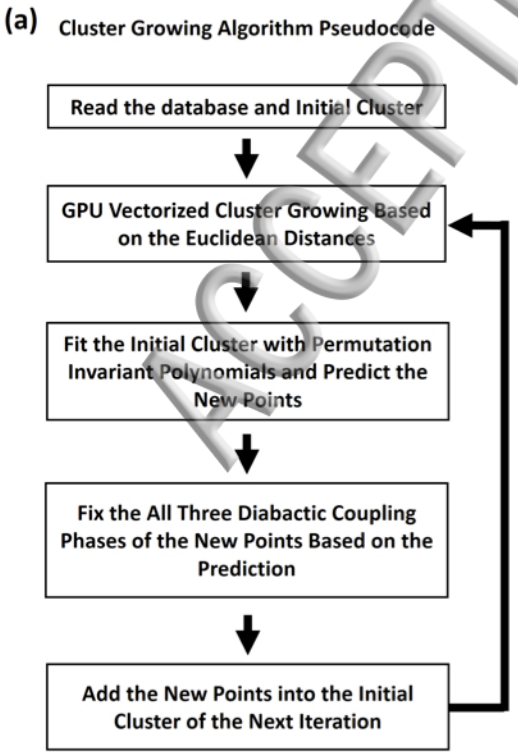
(a)
Cluster Growing Algorithm Pseudocode
Read the database and Initial Cluster
GPU Vectorized Cluster Growing Based on the Euclidean Distances
Fit the Initial Cluster with Permutation Invariant Polynomials and Predict the New Points
Fix the All Three Diabactic Coupling Phases of the New Points Based on the Prediction
Add the New Points into the Initial Cluster of the Next Iteration

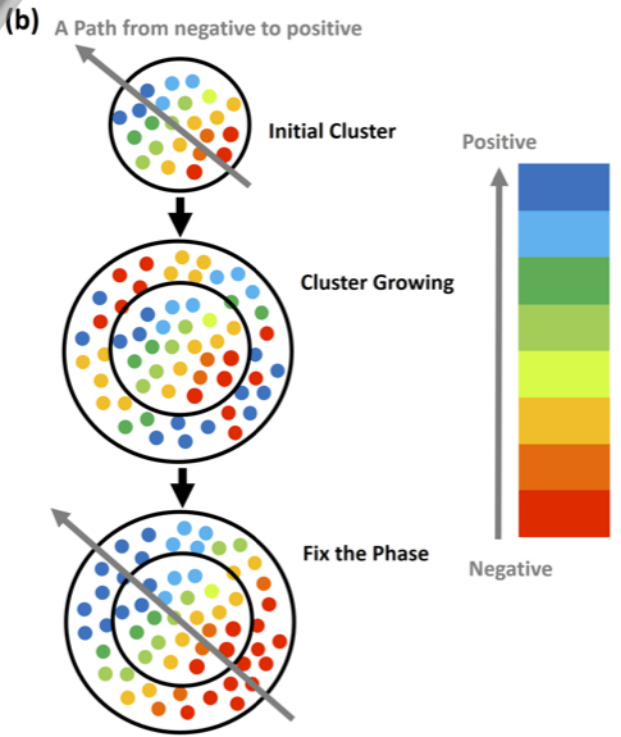
(b)
A Path from negative to positive
Initial Cluster
Cluster Growing
Fix the Phase
Positive
Negative

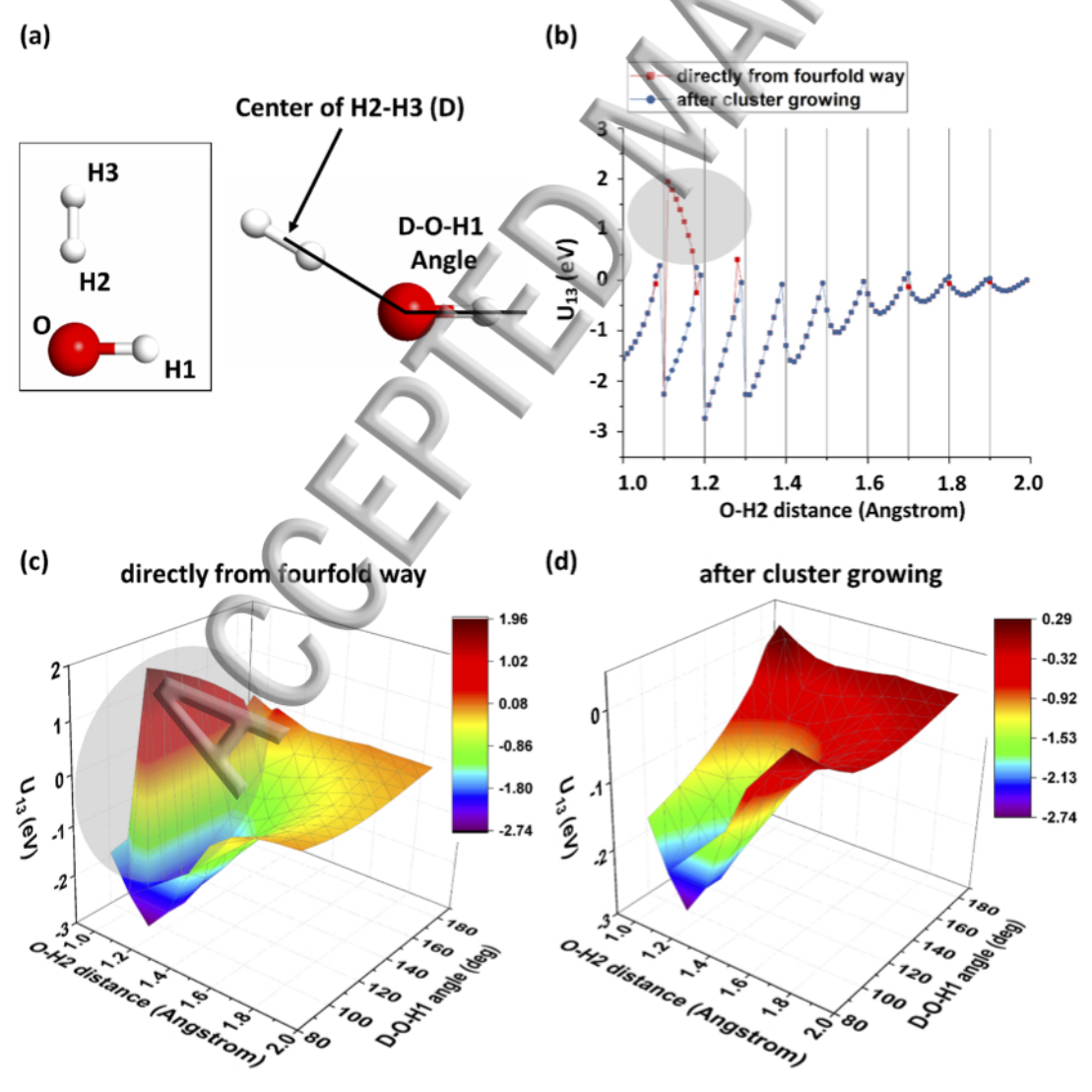

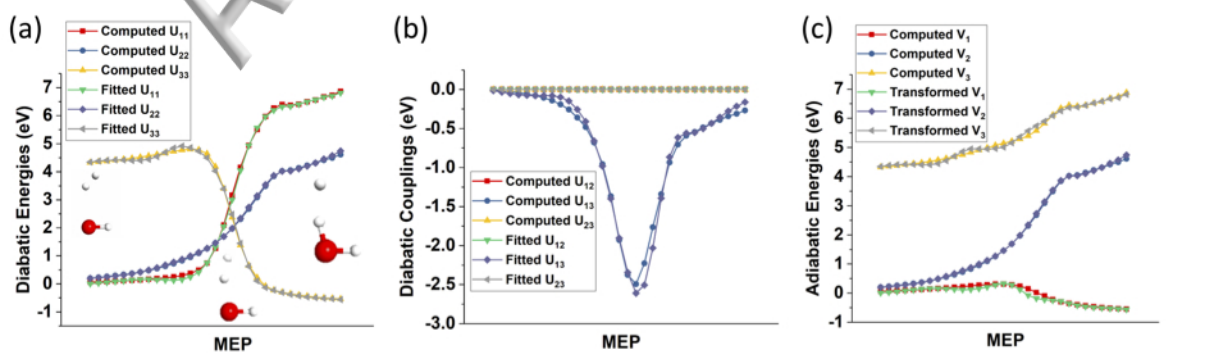
(a)
Computed U_{11}
Computed U_{22}
Computed U_{33}
Fitted U_{11}
Fitted U_{22}
Fitted U_{33}
Diabatic Energies (eV)
MEP
(b)
Computed U_{12}
Computed U_{13}
Computed U_{23}
Fitted U_{12}
Fitted U_{13}
Fitted U_{23}
Diabatic Couplings (eV)
MEP
(c)
Computed V_1
Computed V_2
Computed V_3
Transformed V_1
Transformed V_2
Transformed V_3
Adiabatic Energies (eV)
MEP

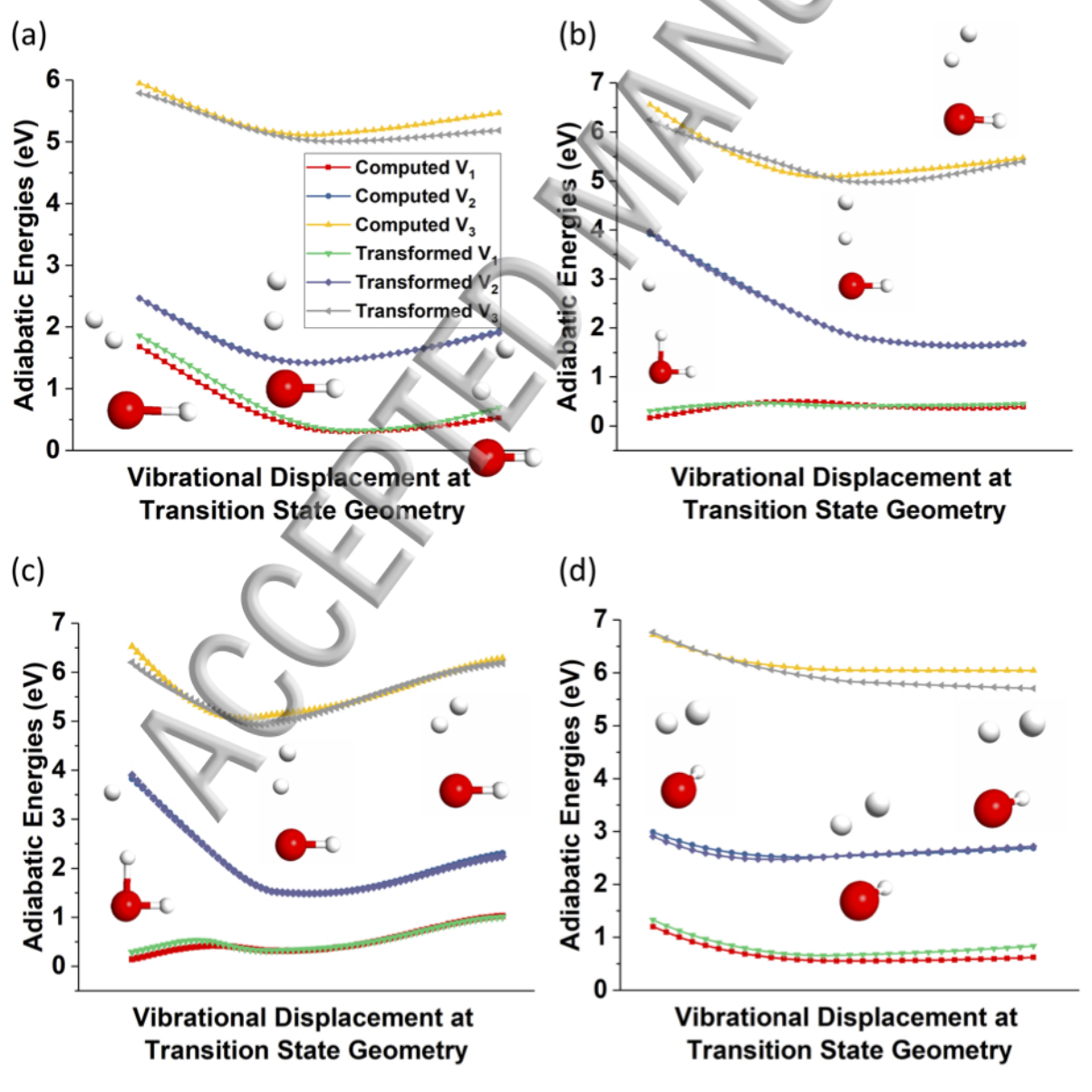

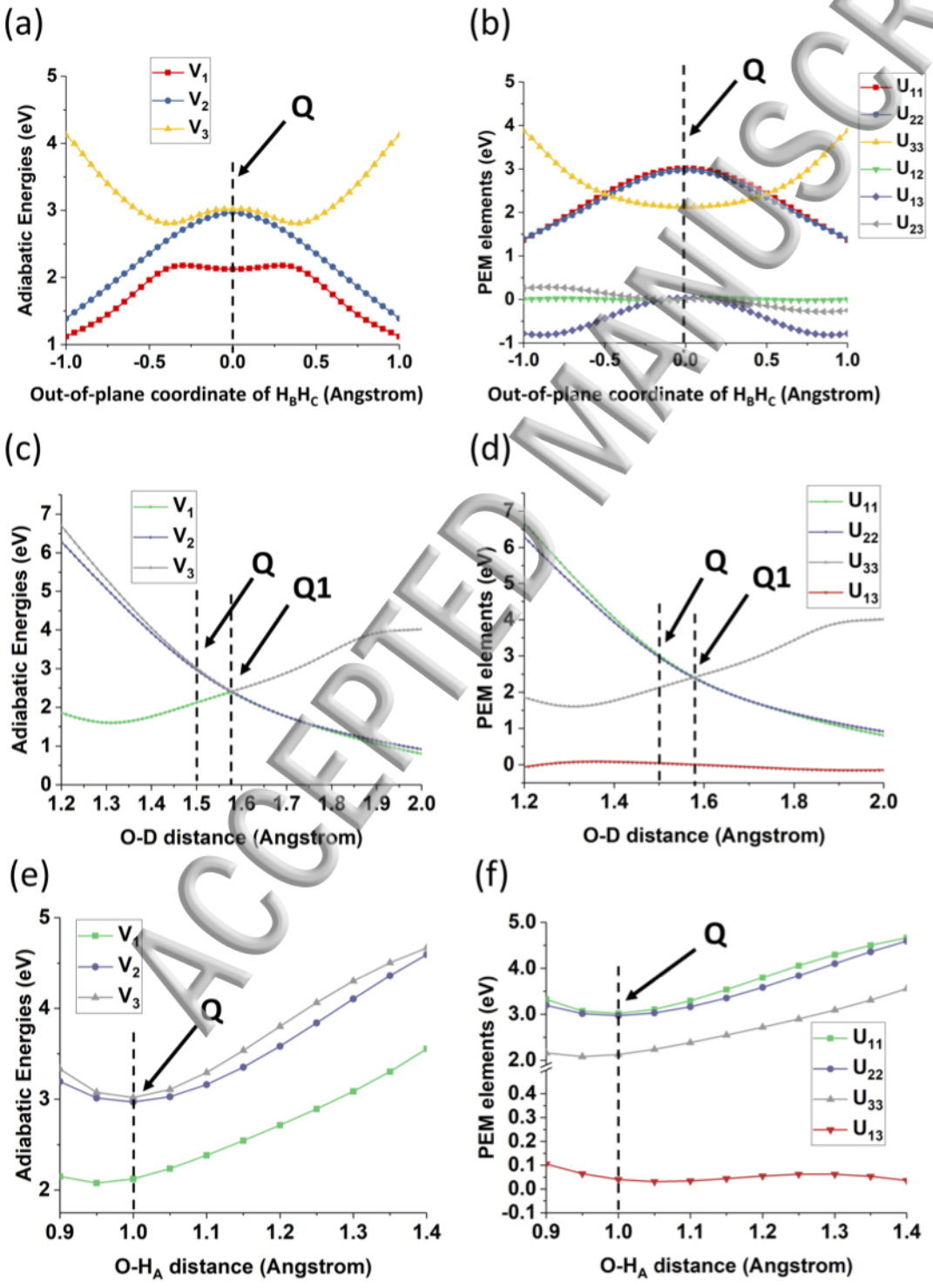

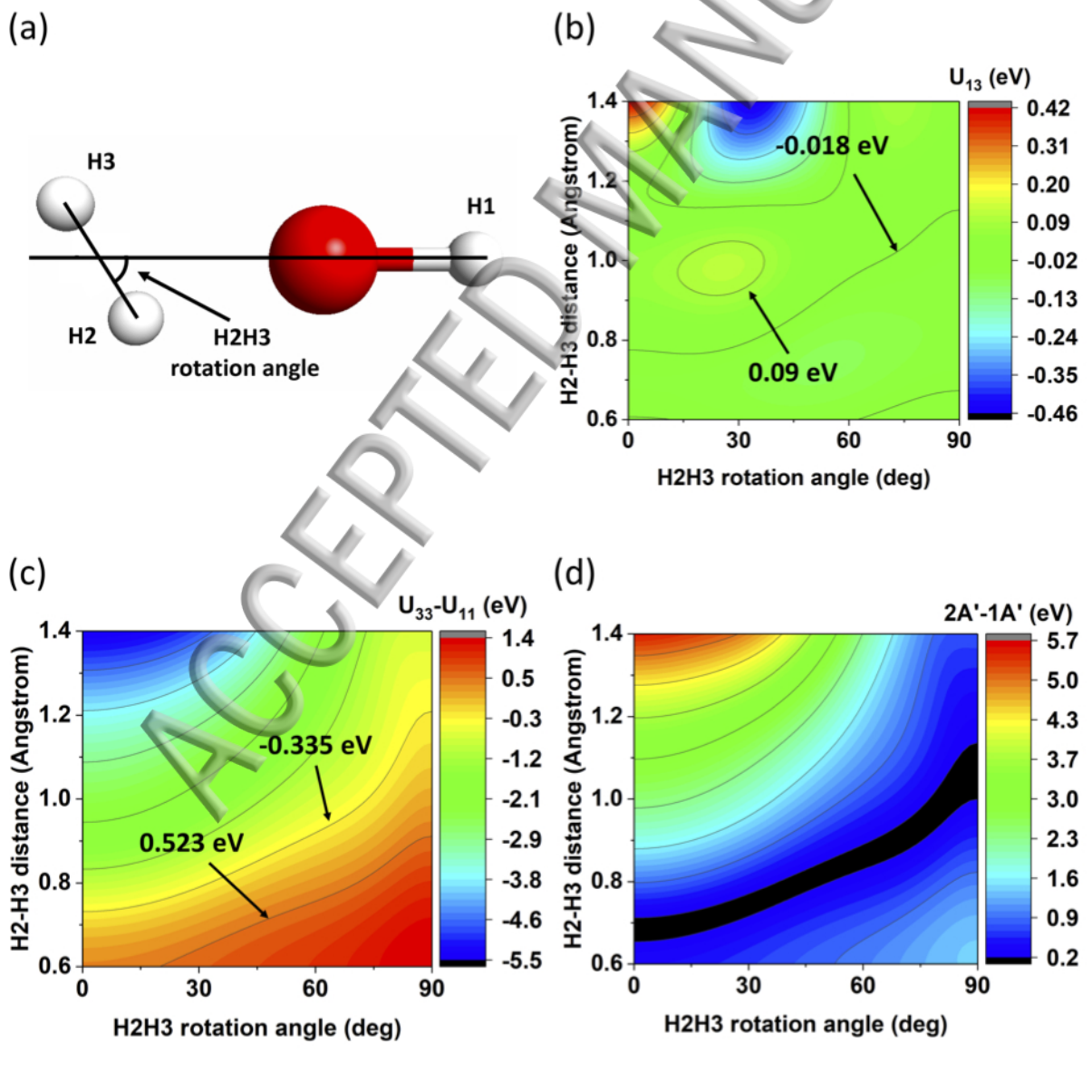

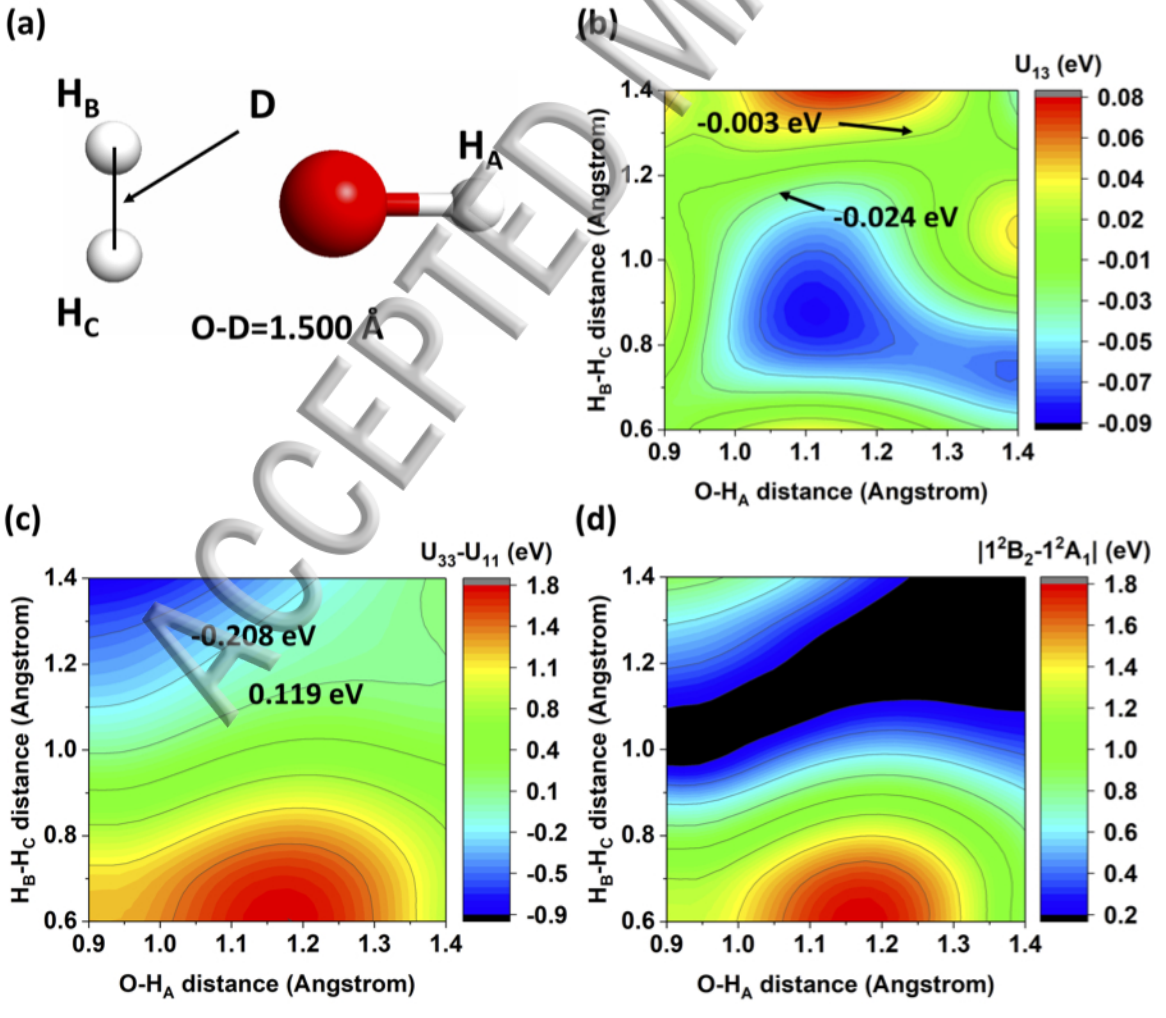
(a)
H_B
D
H_A
H_C
O-D=1.500 Å
(b)
U_13 (eV)
-0.003 eV
-0.024 eV
H_B-H_C distance (Angstrom)
O-H_A distance (Angstrom)
(c)
U_33-U_11 (eV)
-0.208 eV
0.119 eV
H_B-H_C distance (Angstrom)
O-H_A distance (Angstrom)
(d)
|1²B_2-1²A_1| (eV)
H_B-H_C distance (Angstrom)
O-H_A distance (Angstrom)

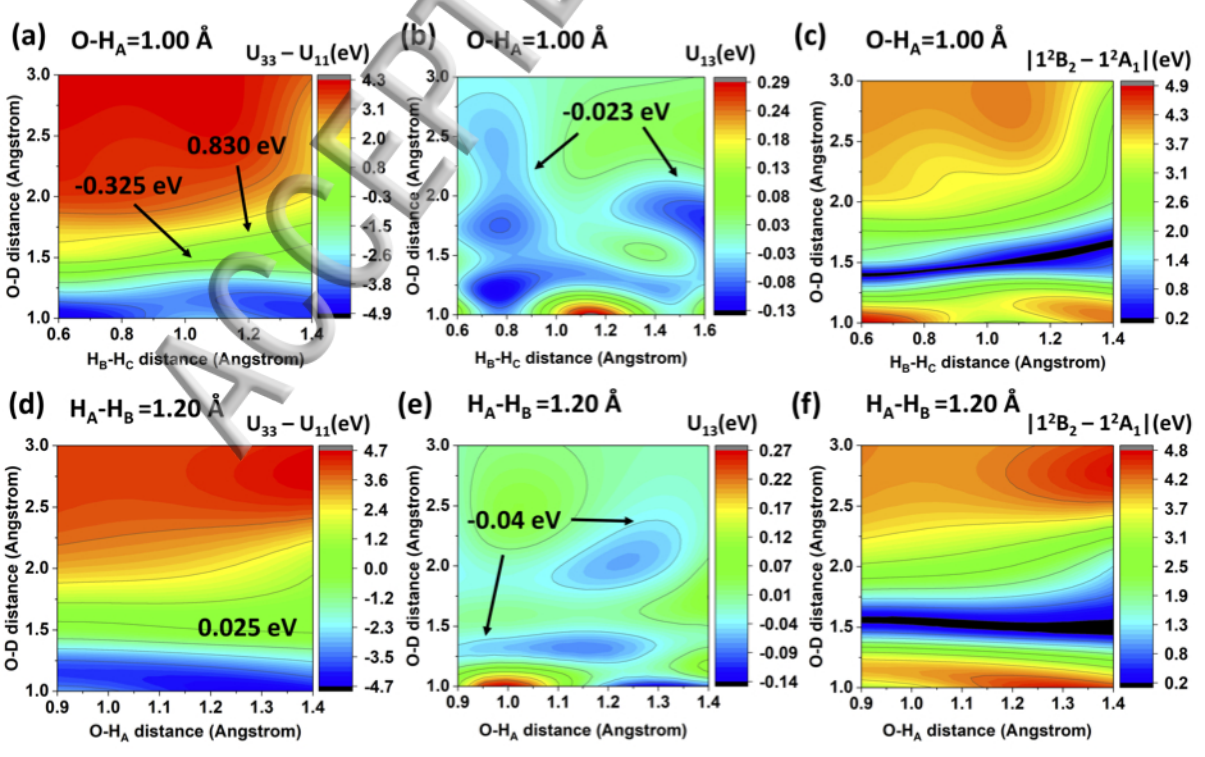
(a)
O-H$_A$=1.00 Å
U$_{33}$ – U$_{11}$(eV)
0.830 eV
-0.325 eV
O-D distance (Angstrom)
H$_B$-H$_C$ distance (Angstrom)
(b)
O-H$_A$=1.00 Å
U$_{13}$(eV)
-0.023 eV
O-D distance (Angstrom)
H$_B$-H$_C$ distance (Angstrom)
(c)
O-H$_A$=1.00 Å
|1^{2}B$_2$ – 1^{2}A$_1$|(eV)
O-D distance (Angstrom)
H$_B$-H$_C$ distance (Angstrom)
(d)
H$_A$-H$_B$ =1.20 Å
U$_{33}$ – U$_{11}$(eV)
0.025 eV
O-D distance (Angstrom)
O-H$_A$ distance (Angstrom)
(e)
H$_A$-H$_B$ =1.20 Å
U$_{13}$(eV)
-0.04 eV
O-D distance (Angstrom)
O-H$_A$ distance (Angstrom)
(f)
H$_A$-H$_B$ =1.20 Å
|1^{2}B$_2$ – 1^{2}A$_1$|(eV)
O-D distance (Angstrom)
O-H$_A$ distance (Angstrom)

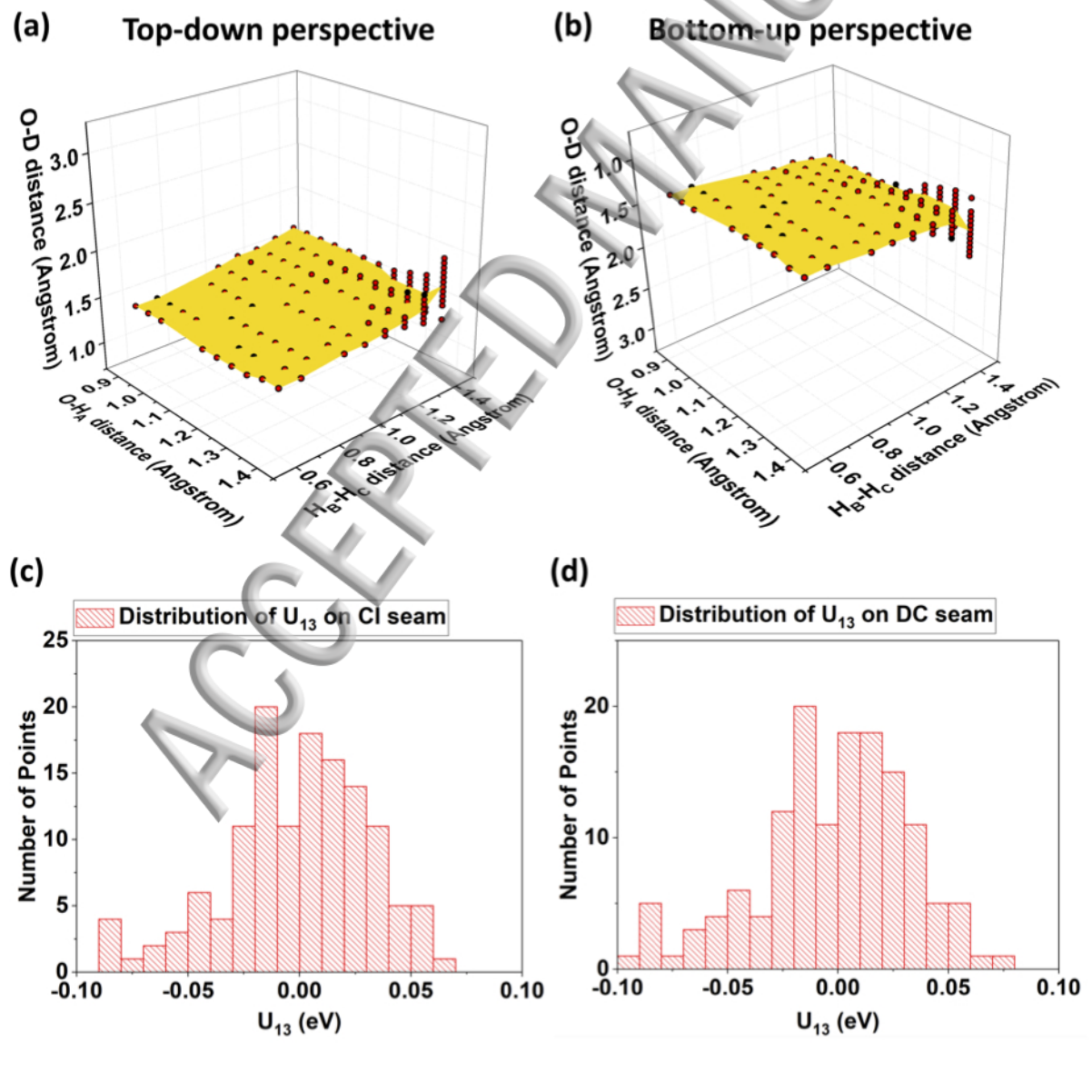

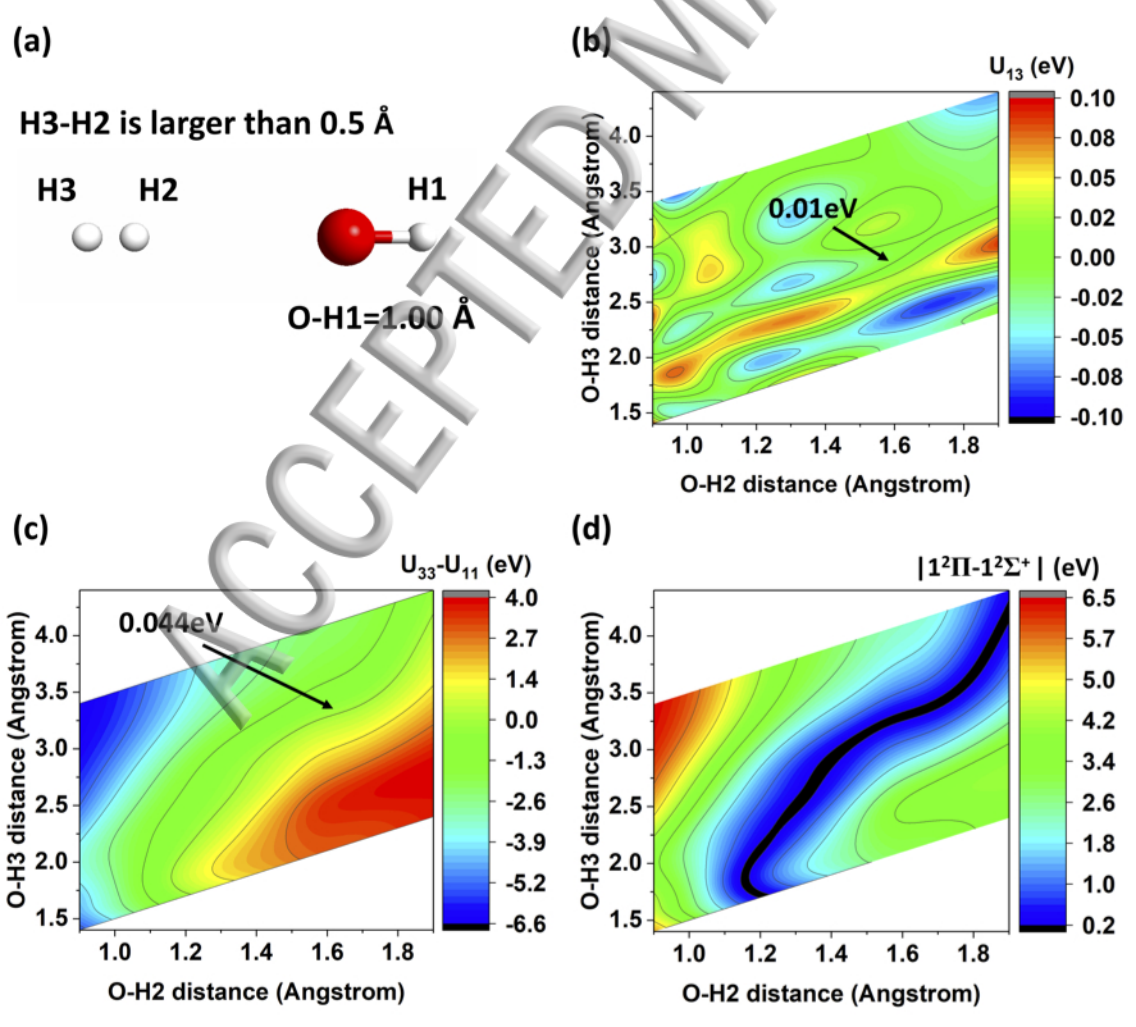
(a)
H3-H2 is larger than 0.5 Å
H3
H2
H1
O-H1=1.00 Å
(b)
U13 (eV)
0.10
0.08
0.05
0.02
0.00
-0.02
-0.05
-0.08
-0.10
0.01eV
O-H3 distance (Angstrom)
O-H2 distance (Angstrom)
(c)
U33-U11 (eV)
4.0
2.7
1.4
0.0
-1.3
-2.6
-3.9
-5.2
-6.6
0.044eV
O-H3 distance (Angstrom)
O-H2 distance (Angstrom)
(d)
|1²Π-1²Σ⁺| (eV)
6.5
5.7
5.0
4.2
3.4
2.6
1.8
1.0
0.2
O-H3 distance (Angstrom)
O-H2 distance (Angstrom)

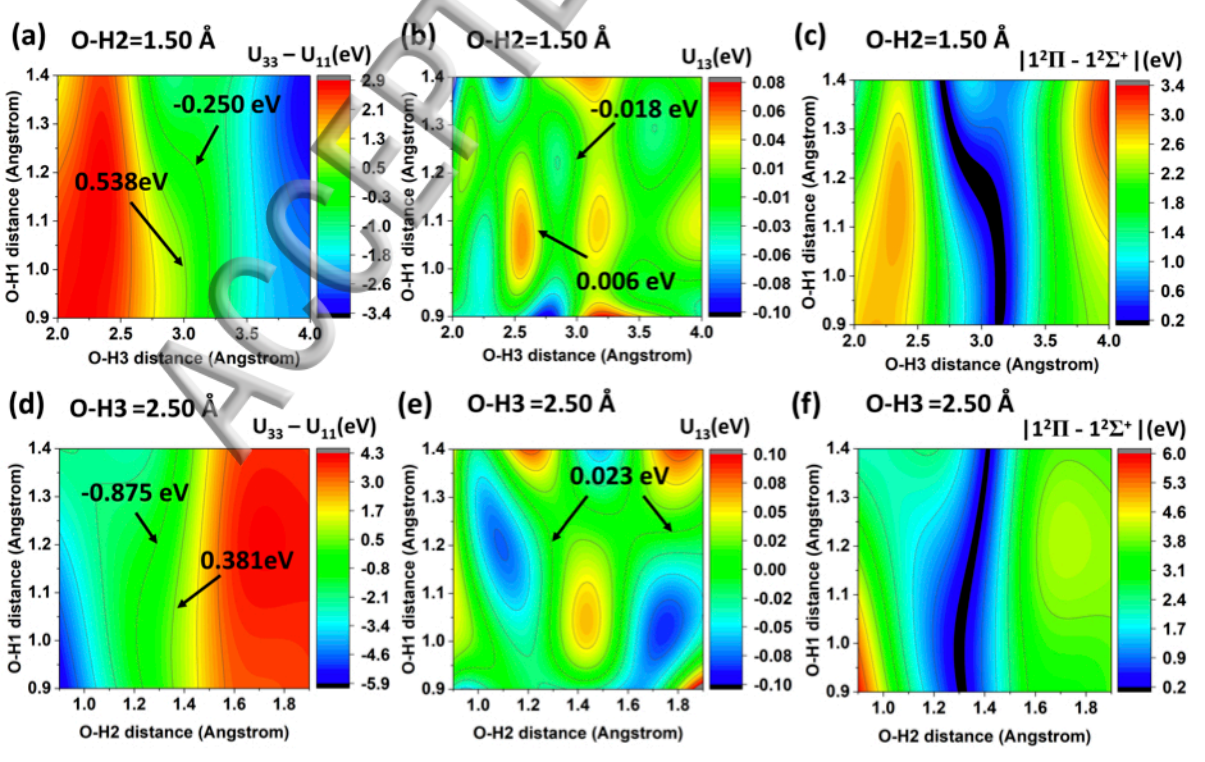
(a)
O-H2=1.50 Å
U33 – U11(eV)
-0.250 eV
0.538eV
O-H1 distance (Angstrom)
O-H3 distance (Angstrom)
(b)
O-H2=1.50 Å
U13(eV)
-0.018 eV
0.006 eV
O-H1 distance (Angstrom)
O-H3 distance (Angstrom)
(c)
O-H2=1.50 Å
|1²Π - 1²Σ⁺|(eV)
O-H1 distance (Angstrom)
O-H3 distance (Angstrom)
(d)
O-H3 =2.50 Å
U33 – U11(eV)
-0.875 eV
0.381eV
O-H1 distance (Angstrom)
O-H2 distance (Angstrom)
(e)
O-H3 =2.50 Å
U13(eV)
0.023 eV
O-H1 distance (Angstrom)
O-H2 distance (Angstrom)
(f)
O-H3 =2.50 Å
|1²Π - 1²Σ⁺|(eV)
O-H1 distance (Angstrom)
O-H2 distance (Angstrom)

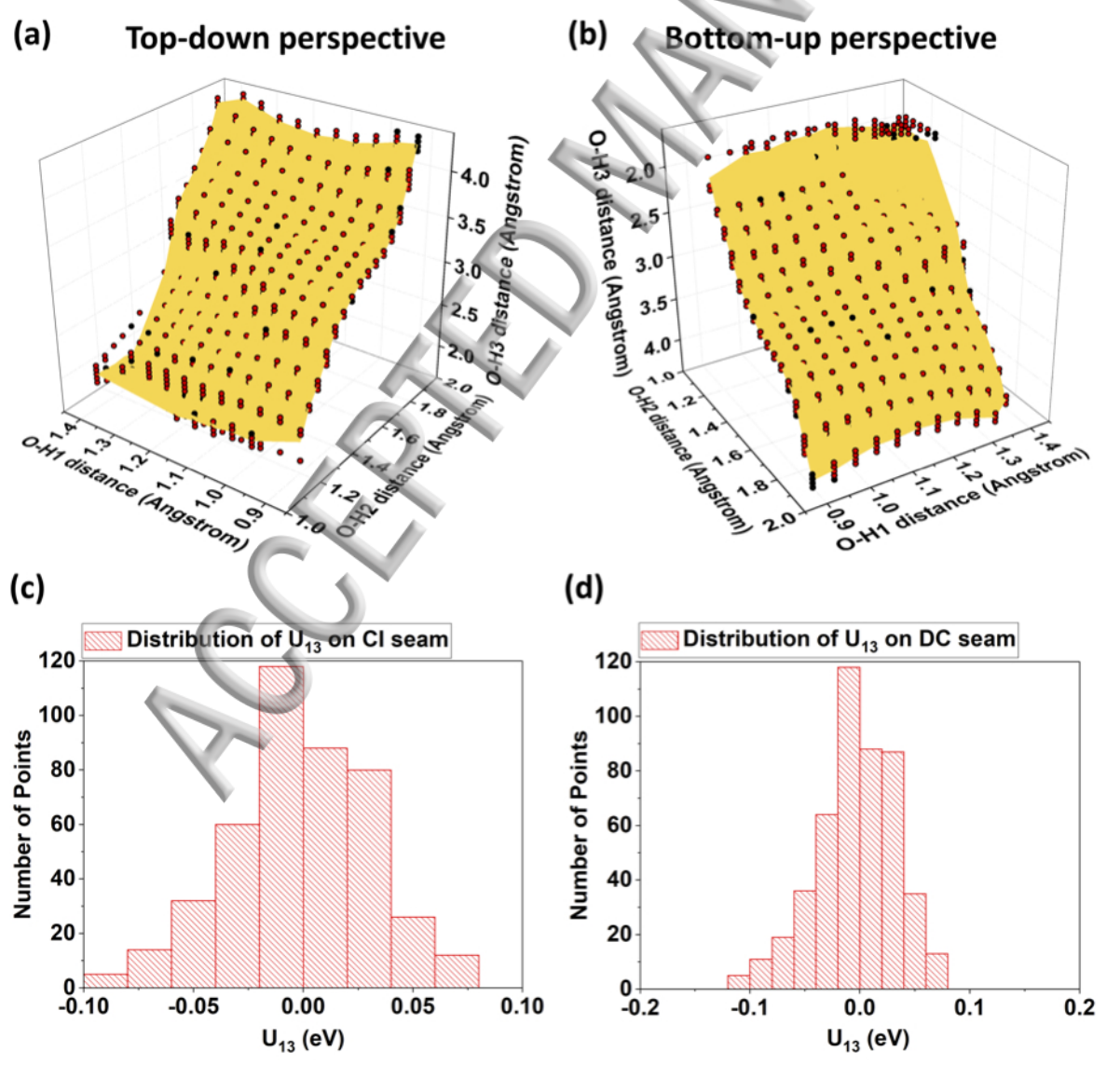

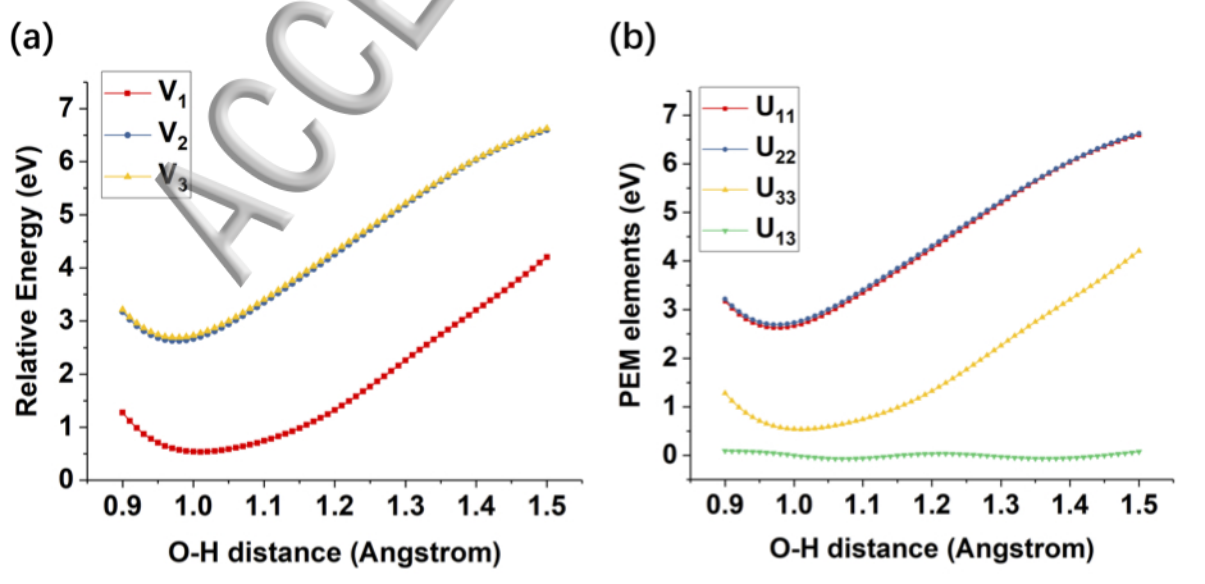
(a)
Relative Energy (eV)
V1
V2
V3
0
1
2
3
4
5
6
7
0.9
1.0
1.1
1.2
1.3
1.4
1.5
O-H distance (Angstrom)
(b)
PEM elements (eV)
U11
U22
U33
U13
0
1
2
3
4
5
6
7
0.9
1.0
1.1
1.2
1.3
1.4
1.5
O-H distance (Angstrom)

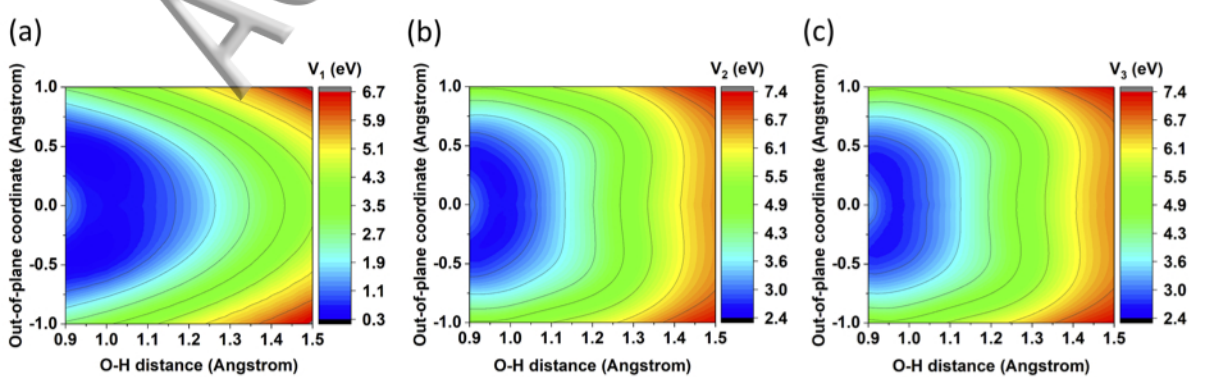
(a)
V1 (eV)
6.7
5.9
5.1
4.3
3.5
2.7
1.9
1.1
0.3
Out-of-plane coordinate (Angstrom)
1.0
0.5
0.0
-0.5
-1.0
0.9
1.0
1.1
1.2
1.3
1.4
1.5
O-H distance (Angstrom)
(b)
V2 (eV)
7.4
6.7
6.1
5.5
4.9
4.3
3.6
3.0
2.4
Out-of-plane coordinate (Angstrom)
O-H distance (Angstrom)
(c)
V3 (eV)
7.4
6.7
6.1
5.5
4.9
4.3
3.6
3.0
2.4
Out-of-plane coordinate (Angstrom)
O-H distance (Angstrom)

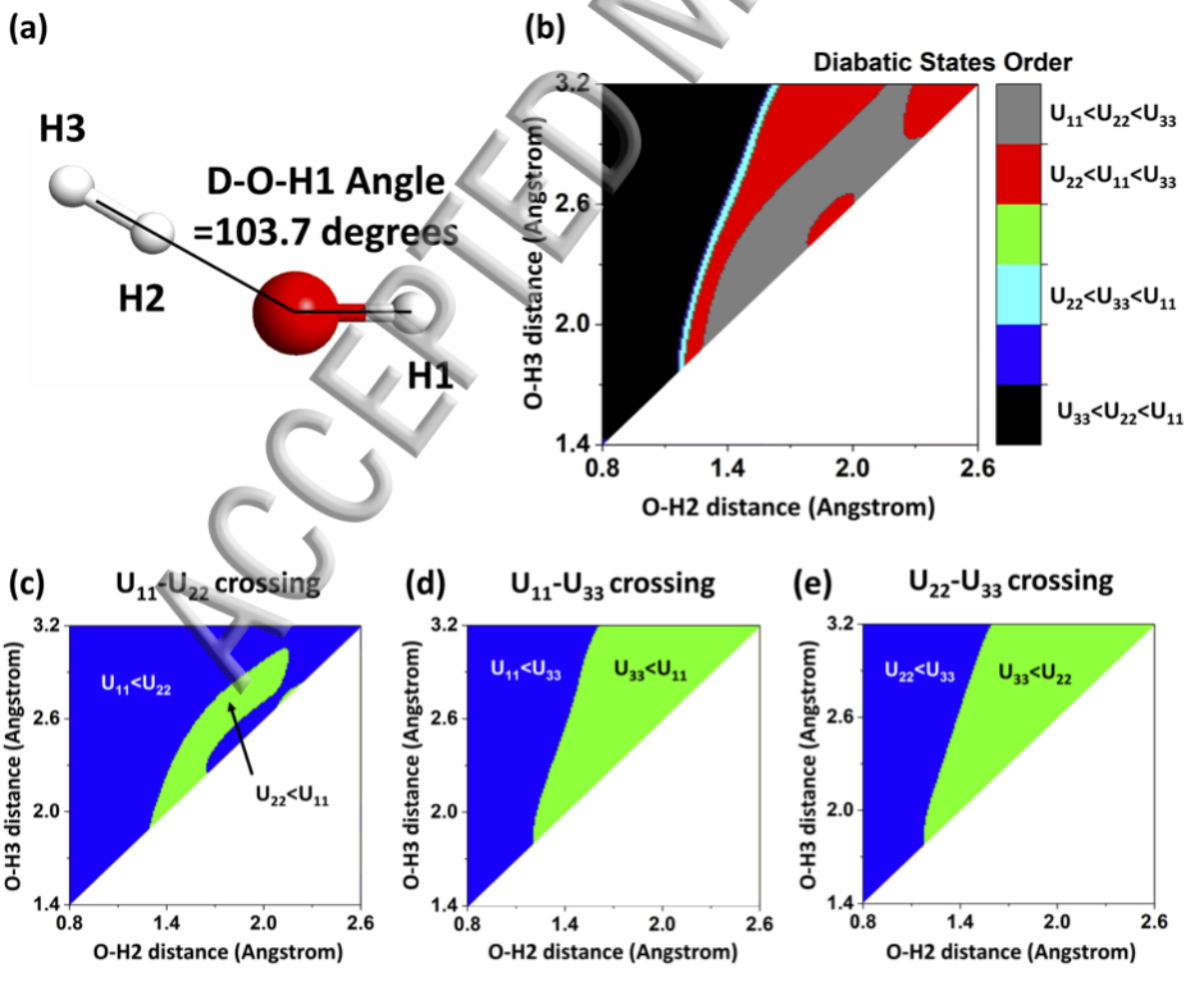

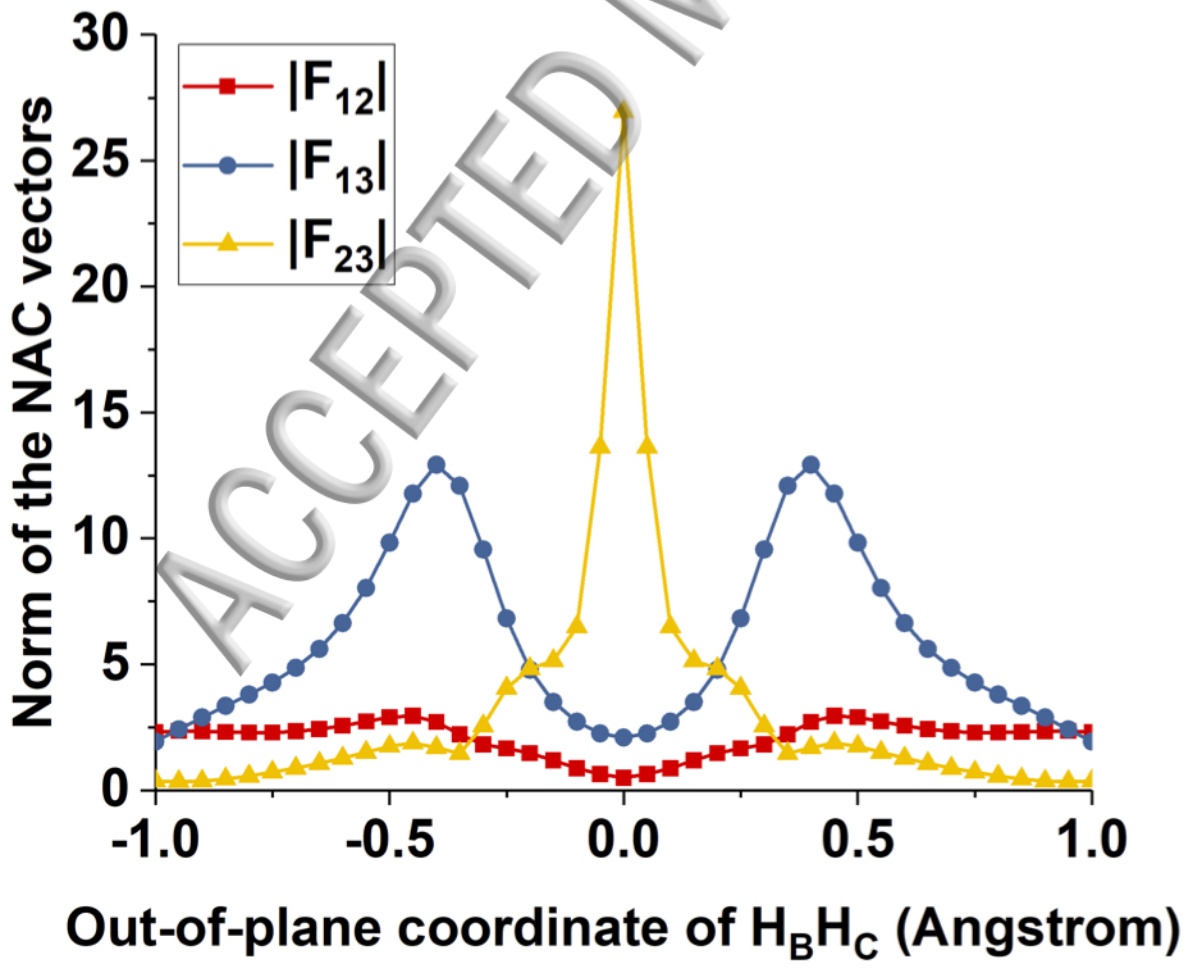
|F12|
|F13|
|F23|
Norm of the NAC vectors
30
25
20
15
10
5
0
-1.0
-0.5
0.0
0.5
1.0
Out-of-plane coordinate of HBHC (Angstrom)

This manuscript was accepted by J. Chem. Phys. Click here to see the version of record. Revised on 1 August 4, 2019

Direct Diabatization and Analytic Representation of Coupled Potential Energy Surfaces and Couplings for the Reactive Quenching of the Excited $^2\Sigma^+$ State of OH by Molecular Hydrogen

Yinan Shu,[1,†] Joanna Kryven,[1,†] Antonio Gustavo Sampaio de Oliveira-Filho,[2,3†] Linyao Zhang,[1] Guo-Liang Song,[1,§] Shaohong L. Li,[1,§§] Rubén Meana-Pañeda,[1,§§§] Bina Fu,[2,4] Joel M. Bowman,[2] and Donald G. Truhlar[1,*]

[1] *Department of Chemistry and Supercomputing Institute, University of Minnesota, Minneapolis, MN 55455-0431, USA*

[2] *Cherry L. Emerson Center for Scientific Computation and Department of Chemistry, Emory University, Atlanta, Georgia 30322, USA*

[3] *Departamento de Química, Laboratório Computacional de Espectroscopia e Cinética, Faculdade de Filosofia, Ciências e Letras de Ribeirão Preto, Universidade de São Paulo, 14040-901, Ribeirão Preto-SP, Brazil*

[4] *State Key Laboratory of Molecular Reaction Dynamics and Center for Theoretical and Computational Chemistry, Dalian Institute of Chemical Physics, Chinese Academy of Sciences, Dalian, 116023, P. R. China*

[†] These authors contributed equally.

[§] Present address: Department of Chemistry, University of Fudan, Shanghai, 200433, China

[§§] Present address: Google, Inc., San Francisco Bay Area, CA

[§§§] Present address: National Institutes of Health, Bethesda, MD 20892-5690

*Corresponding author electronic mail: truhlar@umn.edu

Abstract. We have employed extended multi-configuration quasidegenerate perturbation theory, fourfold-way diabatic molecular orbitals, and configurational uniformity to develop a global three-state diabatic representation of the potential energy surfaces and their couplings for the electronically nonadiabatic reaction $OH^* + H_2 \rightarrow H_2O + H$, where * denotes electronic excitation to the $A\,^2\Sigma^+$ state. To achieve sign consistency of the computed diabatic couplings, we developed a GPU-accelerated algorithm called the cluster-growing algorithm. Having obtained consistent signs of the diabatic couplings, we fit the diabatic matrix elements (which consist of the diabatic potentials and the diabatic couplings) to analytic representations. Adiabatic potential energy surfaces are generated by diagonalizing the 3×3 DPEM. The comparisons between the fitted and computed diabatic matrix elements and between the originally computed adiabatic potential energy surfaces and those generated from the fits indicate that the current fit is accurate enough for dynamical studies, and it may be used for quantal or semiclassical dynamics calculations.

I. INTRODUCTION

The reactions

$$OH(A\ ^2\Sigma^+) + H_2 \rightarrow H_2O + H \quad (1)$$

and

$$OH(A\ ^2\Sigma^+) + H_2 \rightarrow OH(X\ ^2\Pi) + H_2 \quad (2)$$

provide enticing targets for theoretical study because of the detailed experimental data available, dating back to the pioneering experimental studies in the Lester[1,2,3,4], Crosley,[5,6,7] and Heard[8] laboratories. These experiments were motivated in part by the necessity to know the rates and mechanisms of the collisional quenching of electronically excited OH radicals because the quenching affects the laser-induced fluorescence (LIF) measurements of their ground state populations, since LIF on the well characterized $A\ ^2\Sigma^+–X\ ^2\Pi$ band system has often been used[6,9] to detect the hydroxyl radicals, an important species in atmospheric[10,11] and combustion[12] environments. Upon the $A\ ^2\Sigma^+–X\ ^2\Pi$ excitation of isolated OH, only radiative decay is conceivable, but collisions with other molecules open nonradiative de-excitation pathways,[13] such as reactions (1) and (2). The evolution of the electronic states along the reaction path may be seen in Figure 1 (the details of this figure will be explained later, in section III.B.3). Understanding these competitive pathways is necessary to fully interpret the LIF measurements. In addition, the OH_3 system has established itself as the four-body system most widely studied by quantum mechanical dynamics calculations. (OH_3 is a prototype for four-body quantum dynamics in a similar way to how H_3 is a prototype for three-body quantum dynamics.)

Conical intersections have been shown to be ubiquitous[14,15,16,17,18,19,20] on polyatomic potential energy surfaces (PESs). Theoretical studies of the OH_3 system have been largely focused on locating and characterizing the conical intersections that enable nonradiative dynamical pathways by coupling the ground and excited states. Neglecting spin-orbit coupling, we expect the system to show conical intersections in a four-dimensional subspace, Hoffman and Yarkony found conical intersections in $C_{\infty v}$, C_{2v}, and C_s symmetries.[21] Including spin-orbit coupling lowers the dimensionality of the intersection,[22] and Matsika and Yarkony characterized a portion of the seam including spin-orbit coupling.[23]

In an experiment that would be very interesting to simulate, Ortiz-Suárez et al.[24] studied

the reactive quenching of OH ($A\ ^2\Sigma^+$, $v = 0$) by D_2 and found that the product D atoms are primarily forward scattered relative to the incident D_2 and with ~88% of the available energy appearing in HOD internal excitation. Pollack et al.[25] also studied the collisional quenching of OH ($A\ ^2\Sigma^+$) by D_2, and they found nonstatistical OH product distributions. Dempsey et al.[26,27] reported a combined experimental and theoretical study of the nonreactive quenching of OH ($A\ ^2\Sigma^+$) by H_2, and they found high rotational excitation of H_2; the theoretical analysis was limited to nonreactive scattering. Related experimental work[28] probed the partitioning between reactive and nonreactive pathways. Wheeler et al.[29,30] studied mode-selective dynamics of reactions starting from the entrance-arrangement complexes. Kamarchik et al.[31,32,33,34] fitted potential energy surfaces (PESs) to adiabatic potential energy surfaces calculated by multi-reference configuration interaction singles and doubles method plus a quadruples correction (MRCISD+Q), and they studied the post-quenching dynamics with electronically adiabatic trajectories with adiabatic and diabatic choices of initial momenta; this was described as preliminary to coupled-surface dynamics which are required for a complete treatment because the system involves closely coupled states, but the study was prompted by the interesting experimental data and the lack at that time of coupled PESs.

The coupled potential energy surfaces and their couplings required for a more complete theoretical treatment may be generated in either the adiabatic or diabatic representation. Zhang et al.[35,36] reported the first quantum mechanical dynamics study of the electronically nonadiabatic chemical reaction. The calculations were performed on a set of MRCISD coupled PESs; a back propagation neural network was utilized to fit the diabatic PESs and couplings, but the details of the diabatization, the fits, and the PESs were described only briefly in the supplementary material. Dillon and Yarkony[37,38] studied the conical intersection seam with MRCISD calculations, and on the basis of these studies suggested a new mechanism for the quenching. Full-dimensional global diabatic PESs for the three lowest electronic states of the OH + H_2 system have been constructed by Collins and coworkers[39] by an interpolation and new kind of diabatization of MRCI ab initio data; good agreement with the experiment[24] in the distributions of kinetic energy and scattering angle to HOD + H products was obtained. Ma et al.[40] studied the nature of the interaction PESs for fixed values of the OH and H_2 bond distances. A 2014 review by Lehman and Lester[13] concluded that

"still needed are quantum scattering and/or classical dynamics calculations to evaluate quenching cross sections, branching between multiple reactive and nonreactive channels, and the quantum state and kinetic energy distributions of the products."

The objective of present work is to calculate full-dimensional global diabatic PESs and couplings for the three lowest electronic states for reactions (1) and (2) and their representation in a new form that is convenient for dynamics simulations by either quantal or semiclassical methods.

II. BACKGROUND AND NOTATION

In this section, we provide background on diabatization and introduce the language and notation that we use in the rest of the article.

We define an electronically diabatic representation as one for which the coupling due to nuclear momentum and nuclear kinetic energy operating on the wave functions representing the states is assumed to be negligible as compared to coupling due to the electronic Hamiltonian.[41,42] The electronic wave function of state i in an adiabatic representation is called Ψ_i, and the electronic wave function of state i in a diabatic representation is called Φ_i. We assume all wave functions are real; this is always possible when one neglects spin-orbit coupling. When using the adiabatic representation, the potential energies for nuclear motion in electronic state i are the expectation values of the electronic Hamiltonian $H_{\rm el}$ (including, as is conventional, the nuclear repulsion). These are the diagonal elements of a matrix **V** with the elements

$$V_{ij} = \left\langle \Psi_i \middle| H_{\rm el} \middle| \Psi_j \right\rangle \tag{3}$$

where, for $i \neq j$, $V_{ij} = 0$. Hence, we will simply use V_i to represent V_{ii}. When using the diabatic representation, the nuclear motion is governed by a nondiagonal matrix **U** with the elements

$$U_{ij} = \left\langle \Phi_i \middle| H_{\rm el} \middle| \Phi_j \right\rangle \tag{4}$$

The diagonal elements of this diabatic potential energy matrix (DPEM) are the diabatic potential energy surfaces, and the off-diagonal elements are called diabatic couplings. In our

work, we consider diabatic states that span the same space as the directly calculated adiabatic states of interest; we label diabatic bases with this property as adiabatic-equivalent. For such a basis, diagonalizing **U** by an orthogonal transformation yields the adiabatic potential energy surfaces. Because our final diabatic potentials are obtained by *fitting* the adiabatic equivalent ones, the adiabatic potentials obtained by diagonalizing the fitted **U** are not identical to the original adiabatic surfaces, and they are called transformed adiabatic surfaces. But if the fit is good, the transformed adiabatic energies will be good approximations to the originally calculated adiabatic ones.

In discussing the wave functions, potentials, and couplings, it will be convenient to distinguish three regions of configuration space, in particular the reactant-like region (the region corresponding OH + H_2 and OH* + H_2), the tricoordinate region (with ammonia-like geometries), and the product-like region (H_2O + H region). In some parts of the presentation we will label the three hydrogen atoms as H_A, H_B, and H_C based on the O-H distances (r) such that $r(OH_A) \le r(OH_B) \le r(OH_C)$.

We will discuss permutational symmetry in terms of elementary transpositions and cyclic permutations. An elementary transposition is a pairwise permutation of the coordinates of two nuclei. A cyclic permutation can be written as the product of two elementary transpositions.

The concept of an adiabatic PES arises from the Born–Oppenheimer separation of electronic and nuclear motion. Adiabatic PESs are associated with adiabatic electronic states, which are eigenstates of the electronic Hamiltonian for a given set of nuclear coordinates, i.e., a given geometry. Adiabatic PESs are obtained by performing electronic structure calculations to obtain approximations to the adiabatic electronic wave functions and energies. The electronic states are coupled by nuclear momentum and nuclear kinetic energy operators; one often makes the semiclassical approximation that only the former are considered,[43,44] and these are called nonadiabatic coupling vectors or nonadiabatic couplings (NACs). For small systems one can also employ direct dynamics in which adiabatic energies, gradients, and NACs are generated by electronic structure calculations whenever they are needed by the dynamics algorithm, but the high expense of reliable electronic structure methods usually leads users of adiabatic representations to using lower levels of theory, less exploration of

initial-state space, and short-time simulations. These shortcomings can be overcome by employing analytically fitted surfaces[45,46] or interpolation.[47,48,49,50] Fitting and interpolation are essentially impossible in the adiabatic representation because of cuspidal behavior of the PESs and singular behavior of the NACs at multidimensional conical intersection seams; this motivates the use of diabatic representations, for which the DPEMs (consisting of diabatic PESs and diabatic couplings) are smooth scalars. In the present work we will calculate and fit DPEMs.

Diabatic states are not uniquely defined,[41,42] and there have been many schemes proposed to construct diabatic states.[51,52,53,54,55,56,57,58,59,60,61,62,63,64,65,66,67,68,69,70,71,72,73] In the present work, we applied the fourfold-way,[60,63,64] which is based on the principle of configurational uniformity.[57] The fourfold-way has been previously applied to several systems, including bromoacetyl chloride,[74] ammonia,[75,76] phenol,[77,78,79] thioanisole,[80] and thiophenol.[81] A difference of the present work from these calculations is that they provided at most semiglobal DPEM, for example the DPEM for a range of geometries centered on the lowest-energy dissociation path, whereas the present calculations provide a fully global potential energy surface that describes all possible geometries reasonably well (at least that is the goal). After the DPEM is obtained, dynamics calculations can be performed in either the diabatic or the adiabatic representation because the generation of the adiabatic surfaces and NACs corresponding to a given diabatic approximation is straightforward.[82]

III. ADIABATIC AND DIABATIC ELECTRONIC WAVE FUNCTIONS OF OH_3

III.A. Adiabatic Electronic Wave Functions. In the present work, our goal is to obtain a diabatic basis equivalent to the three lowest-energy adiabatic states of the OH_3 system. At the reactant asymptote these states correspond to the doubly degenerate X $^2\Pi$ state and the A $^2\Sigma^+$ state of the OH molecule. The energies and wave functions of these states are calculated by extended multi-configuration quasidegenerate perturbation theory (XMC-QDPT).[83,84,85,86] The XMC-QDPT calculations are based on state-averaged complete-active-space self-consistent field (SA-CASSCF)[87] wave functions as the reference states. The one-electron basis set on the O atom is the cc-pVTZ basis[88] with two additional evenly tempered diffuse s and p subshells, and the basis set on the H atom is unaugmented cc-pVTZ.

The SA-CASSCF wave function is obtained as a state average of the three lowest adiabatic doublet states of the OH_3 system, and the energies of these states are averaged with equal weights. The active space consists of 9 electrons in 11 orbitals. This is based mainly on the extended correlated participating orbitals (*ext*-CPO) scheme.[89] While the three original CPO schemes[89] work well for generating smooth semiglobal PESs, for example, from one asymptote to another along a particular reaction path, further supplementation of the *ext*-CPO active space with an extra orbital is needed here to both account for symmetry along the C_{2v} pathways connecting the tricoordinate region to the product (H_2O + H) region and to provide a more balanced treatment across the global PESs that include high-energy asymptotes. Therefore we added another orbital to the *ext*-CPO choice. Thus the active space used is comprised of the 10 orbitals of the *ext*-CPO scheme plus one 3*d* orbital on the O atom. The eleven active orbitals are as follows: (i) in the OH + H_2 region, they are the σ and σ^* orbitals describing the OH bond, σ and σ^* orbitals describing the HH bond, the 2*s*, 3*s*, $2p_y$, $2p_z$, $3p_y$, and $3p_z$ orbitals of the oxygen atom (where the orientations of the *x*, *y*, and *z* axes are discussed below), and the 3*d* orbital on the oxygen; (ii) in the tricoordinate region, they are the 2*s*, 3*s*, $2p_z$, and $3p_z$ orbitals on the O atom, an orbital resulting from an anti-bonding combination of the oxygen 3*s* and the three hydrogen 1*s* orbitals (a totally symmetric orbital in D_{3h}), and the three lowest pairs of orbitals that become $e_{p_{x,y}}$ at D_{3h} geometries; (iii) in the H_2O + H region, they are the $1b_2$, $2a_1$, $1b_1$, $3a_1$, $2b_2$, $4a_1$, $2b_1$, $5a_1$, and $6a_1$ orbitals of the water molecule, one oxygen *d* orbital, and a 1*s* orbital on the separated H; and (iv) in the limit of four separated atoms they are the 2*s*, 3*s*, $2p_y$, $2p_z$, $3p_y$, $3p_z$, $2p_x$, $3p_x$ orbitals on the O atom and the 1*s* orbitals on each of the three H atoms. This active space, which we call *ext*-CPO$^+$, was found to be adequate to provide realistic PESs globally.

All electrons except the oxygen 1s orbital are correlated in the XMC-QDPT perturbation theory treatment. To avoid artifacts due to the possibility of intruder states in the XMC-QDPT wave function, the intruder state avoidance method (ISA)[90] was consistently applied at all molecular configurations; the level shift parameter *b* of the ISA method was set to 0.02 E_h, where E_h denotes a hartree atomic unit of energy.

Calculations were performed for more than 70000 molecular geometries that consisted

of (i) a set of nuclear configurations generated by trajectory calculations on the lowest adiabatic PES starting from conical intersections in previous work,[31,32,33,34] (ii) a wide variety of regular grids of nuclear configurations generated, for example, along vibrational normal modes at geometries relevant to the experiments, (iii) geometries added by running classical trajectories on individual diabatic PESs analogously to the Grow algorithm proposed by Collins and coworkers[47,48,49] until the fits are considered to be well enough converged, and (iv) additional points near the ground-state reaction path and in the reactant van der Waals region to obtain higher accuracy in those important regions.

III.B. Diabatization. The first step in the fourfold-way is the determination of diabatic molecular orbitals (DMOs). We do this using SA-CASSCF, and further details of this process are given below in Subsection III.B.2. The SA-CASSCF wave functions are originally obtained in terms of adiabatic configuration state functions (CSFs) expressed in terms of adiabatic canonical molecular orbitals. The adiabatic CSF basis is then transformed to basis of diabatic state functions (DSFs, denoted by χ_α) constructed in terms of the DMOs. Each SA-CASSCF adiabatic state is then expressed as a linear combination of the N orthonormal DSFs:

$$\Psi_n = \sum_{\alpha=1}^{N} C_{\alpha n} \chi_\alpha \tag{5}$$

and three diabatic states, Φ_1, Φ_2, and Φ_3, are obtained by orthogonal transformation of the three lowest adiabatic states Ψ_1, Ψ_2, and Ψ_3:

$$\Phi_k = \sum_{n=1}^{3} T_{nk} \Psi_n \tag{6}$$

where T_{nk} is an element of adiabatic-to-diabatic rotation matrix.

After the diabatic states at the SA-CASSCF level are obtained, the model-space diabatization algorithm[91] is used to obtain the diabatic states at the XMC-QDPT level. In particular, Ref. 91 shows that the XMC-QDPT diabatic wave functions obtained from configurational uniformity are equivalent within the CAS-CI space to the SA-CASSCF diabatic wave functions. Therefore, the XMC-QDPT adiabatic-to-diabatic transformation for the three states of interest can be obtained by first transforming the XMC-QDPT model states

back to the SA-CASSCF adiabatic states, and then transforming the SA-CASSCF adiabatic states to the SA-CASSCF diabatic states. The XMC-QDPT adiabatic-to-diabatic transformation is then used to convert the XMC-QDPT adiabatic energies to the diabatic potential matrix. Details were given previously.[91]

III.B.1. Standard orientation. All calculations of the diabatization steps are performed in a standard orientation of the molecule, which is defined as follows: (i) the oxygen atom is placed at the origin; (ii) the positive direction of the *x*-axis coincides with a vector from the origin to the closest hydrogen atom; (iii) the plane containing the oxygen, the closest hydrogen (referred to as A) to the oxygen, and the next closest hydrogen (referred to as B) is assigned as the *xy*-plane; (iv) rotation-reflection operations are then applied so that the *y*-coordinate of B is always positive and the *z*-coordinate of the third closest hydrogen (C) is always positive. This standard orientation is needed because it aligns the molecule in a uniquely defined way with respect to the reference orbital defined in the next subsection.

III.B.2. Diabatic molecular orbitals. The DMOs are obtained by a transformation of the canonical molecular orbitals. In general, the transformation involves a threefold density criterion and a fourth criterion of maximum overlap with one or more reference orbitals, and it is completely described previously[60,63] with the exception of the system-dependent choice of reference orbital or orbitals. The reference orbitals are needed to avoid a rapid change of DMOs in the strong interaction region. Unfortunately there is no systematic way to find suitable reference orbitals, so we use a trial-and-error approach that selects the reference orbital to restrain the orbital switching that we see in its absence. In previous work we have found that a reference orbital is usually needed to sort out two nonbonding *p* orbitals on the same atomic center, and consistent with that experience, we found for the present problem that we could obtain smooth DMOs with only one reference orbital, and that this reference orbital basically serves to keep a p_y-like orbital on oxygen from mixing in an uncontrolled fashion with the other DMOs. The rest of this subsection defines this reference orbital, which is complicated by the necessity to preserve invariance to permutations of the three identical hydrogen atoms because we are developing a fully global DPEM.

The reference orbital is called $\mathbf{u}_3$, and it is defined by rotating and combining two simplified in-plane p_y-like DMOs – one obtained by the threefold density criterion at a

reactant-like geometry, and one obtained by the threefold density criterion at a product-like geometry. The simplified p_y-like DMOs are defined as follows:

The first simplified p_y-like DMO is prepared as follows. The SA-CASSCF optimized p_y-like DMO at reactants (obtained by the threefold density criterion) is simplified to a pure atomic p orbital on the O atom by zeroing the coefficients of the basis functions on other atoms and of the s, d, and f basis functions on the oxygen. (The zeroed coefficients are all very small.) Since we use a valence triple zeta basis set, this leaves twelve nonzero LCAO coefficients in the simplified orbital. This vector is denoted as $\mathbf{v}_3^{(1)}$.

The simplified p_y-like DMO at products is obtained in a similar fashion at the product geometry. In particular we remove the coefficients of the basis functions other than s and p functions on the oxygen and remove all basis functions from the three hydrogen atoms. This vector is denoted $\mathbf{v}_3^{(2)}$.

At each molecular geometry **R** where the DPEM is to be evaluated, the following steps are performed:

(1) A vector $\mathbf{v}_3^{(2,P)}$ that is invariant with respect to the exchange of the identical nuclei is defined by

$$\mathbf{v}_3^{(2,P)} = \sum_{i=1,2,3;j<i} f_{ij}\, \mathbf{v}_{\text{bisector}}^{(2)H_iOH_j} \tag{7}$$

where $\mathbf{v}_{\text{bisector}}^{(2)H_iOH_j}$ is $\mathbf{v}_3^{(2)}$ placed on each of the three HOH bisectors, and the weights f_{ij} are defined as follows:

$$f_{ij} = \frac{e^{-(r_{OH_i}-r_{OH_j})/d^2}}{\sum_{i=1,2,3;j<i} e^{-(r_{OH_i}-r_{OH_j})/d^2}} F_{\mathrm{d}_{ij}} \tag{8}$$

where $d = 0.2$ Å, and the functions $F_{\mathrm{d}_{ij}}$ are used to eliminate the contributions of $\mathbf{v}_3^{(2)}$ at geometries with at least one 180° bond angle. These functions are constructed as:

$$F_{d_{ij}} = \prod_{i=1,2,3;j<i} (1-2e^{-\Delta_{ij}}/(1+e^{-2\Delta_{ij}})) \tag{9}$$

where Δ_{ij} is the deviation in radians of the H_iOH_j angle from π.

(2) The vector $\mathbf{v}_3^{(1,P)}$ is defined as:

$$\mathbf{v}_3^{(1,P)} = (1-S)\mathbf{v}_\perp^{(1),\mathrm{AOB}} + S\mathbf{v}_\perp^{(1),\mathrm{AOC}} \tag{10}$$

where $\mathbf{v}_\perp^{(1),\mathrm{AOB}}$ and $\mathbf{v}_\perp^{(1),\mathrm{AOC}}$ are generated by placing $\mathbf{v}_3^{(1)}$ normal to the OA bond in the AOB and AOC planes respectively, and S is a function that gradually shifts between them as a function of the r_{OB} and r_{OC} distance as they switch,

$$S = \frac{1}{2}\left(\tanh\left[2\left(r_{OB} - r_{OC}\right)\right] + 1\right) \tag{11}$$

Vector $\mathbf{v}_3^{(1,P)}$ is thus invariant with respect to the permutations of the nuclear coordinates of the second and the third farthest from the oxygen H atoms. While the closest A hydrogen atom is not included in the definition of $\mathbf{v}_3^{(1,P)}$, it does not switch with either B or C in the region (reactant channel) where $\mathbf{v}_3^{(1,P)}$ contributes to the final reference orbital.

The final reference DMO is then given by

$$\mathbf{u}_3 = (1-F_p)\mathbf{v}_3^{(1,P)} + F_p\mathbf{v}_3^{(2,P)} \tag{12}$$

where

$$F_p = e^{-(r_{OB}-r_{OA})^2/\tilde{d}^2} \tag{13}$$

and where $\tilde{d} = 0.3$ Å.

With this reference orbital, we computed the final DMOs by the fourfold-way, and their characters are summarized in Table I. In this table, the reference orbital is orbital 3.

III.B.3. Diabatic states. Each diabatic state is identified by a diabatic prototype list, which contains its dominant DSFs. Each DSF is a spin-adapted linear combination of Slater determinants expressed in terms of the DMOs of Table I. The diabatic prototype lists are given in Table II; note that no DSF appears in more than one list, and only DSFs needed to distinguish the diabatic states are included in any of the lists. Figure 1 schematically shows the dominant configurations of the diabatic states in the reactant-like region, in the tricoordinate region, and in the product-like region.

The diabatic prototype list for diabatic state 1 is (χ_1, χ_2, χ_3). In C_s symmetry this state corresponds to the A′ component of the doubly degenerate $X\,^2\Pi$ state of the OH with the singly occupied molecular orbital (SOMO) localized in an oxygen p_y orbital as expressed by DSF χ_2. At products, diabatic state 1 corresponds to the A $^1B_1(1b_1 \rightarrow 3s/4a_1)$ state of water and the ground state of H as expressed by DSF χ_3. In the tricoordinate region, it corresponds to the p_x component of the ^{2}E excited state of OH_3 as prototyped by DSF χ_1.

The diabatic prototype list for diabatic state 2 is (χ_4, χ_5, χ_6). In C_s symmetry this state corresponds to the A′′ component of the doubly degenerate $X\,^2\Pi$ state of the OH radical, with the SOMO localized oxygen at p_z orbital as expressed by DSF χ_4. At the H_2O + H asymptote, it corresponds to the A $^3B_1$ $(1b_1 \rightarrow 3s/4a_1)$ state of water and the ground state of H as expressed by DSF χ_6. In the tricoordinate region, it corresponds to the p_y component of the ^{2}E excited state of OH_3 as expressed by DSF χ_5.

The diabatic prototype list for diabatic state 3 is (χ_7, χ_8). This state corresponds to the A $^2\Sigma^+$ state of OH at the OH + H_2 asymptote where it is dominated by the DSF χ_7 with a (212220000) configuration describing a state with the SOMO localized corresponding to σ_{OH}. At the product asymptote, diabatic state 3 corresponds to the ground state of products H_2O (X $^1A_1$) + H(^{2}S) where it is dominated by the DSF χ_8 with a (222210000) configuration. In the tricoordinate region, this state corresponds to OH_3 ($^2A_1$;3s) where it is also dominated by χ_8.

The diabatic state 3, if prototyped only by DSF χ_7 would have correlated to the high energy H_2O^+ (B $^2B_2$) + H^-(^{1}S) asymptote at the product side, as shown in Fig. 1. Diabatic states 1 and 2, if prototyped only by their dominant CSFs at reactants, χ_2 and χ_4 respectively, would diabatically correlate to the states H_2O^+ (X $^2B_1$) + H^-(^{1}S) and H_2O^+ (A $^2A_1$) + H^-(^{1}S) at the product side. This implies that diabatic states 2 and 3 change their dominant characters along paths beginning in the OH + H_2 region, passing through the tricoordinate region, and ending in the H_2O + H region; this is required if the diabatic states

are to span the same space as the three lowest adiabatic states. The change in character of diabatic state 3 has little effect on the dynamics since it occurs in a high-energy region where the third state is unimportant at the energies of the experimental work reviewed in the introduction. The change in character of the second diabatic state is a more significant approximation of the present treatment; limiting the treatment to three states is potentially one of the most serious approximations of the present treatment, especially in the tricoordinate region. In our experience it often happens that if one uses n adiabatic-equivalent diabatic states, the nth diabatic state may acquire some nonsmoothness because of a conical intersection or locally avoided crossing of adiabatic surfaces n and $n+1$; if this occurs in a dynamically important region, one should add another state. Fortunately, in the present case it does not.

IV. ANALYTICAL FIT OF THE DIABATIC MATRIX ELEMENTS

Our minimal criteria for a useful diabatic representation of potential energy surfaces are: (a) The DPEM should be as smooth as possible within the constraint of maintaining adiabatic equivalence. (b) It should be single-valued. (c) The transformed adiabatic surfaces should agree reasonably well with the originally calculated adiabatic surfaces for those energies that are low enough to be accessible during the planned simulation. We next present a fit designed to satisfy these criteria.

IV.A. Diabatic Potential Energy Surfaces. The six-dimensional diabatic potential energy surfaces are fit to the following functional form

$$V\left(r_1,r_2,r_3,r_4,r_5,r_6\right)=V_0+\sum_i^6 V_{\mathrm{PA}}\left(r_i\right)+V_{\mathrm{MB}} \tag{14}$$

where V_0 a constant that sets the zero of energy at the equilibrium OH+H_2 asymptote, V_{PA} is a two-body term in a pairwise additive sum, and V_{MB} is a many-body term.

For the U_{11} and U_{22} diabatic surfaces and for the HH interaction in U_{33}, the pairwise potentials for H_2 and OH are written as a sum of short- and long-range potentials

$$V_{\mathrm{PA}}\left(r\right)=V_{\mathrm{SR}}\left(r\right)+V_{\mathrm{LR}}\left(r\right) \tag{15}$$

The short-range potentials are given by an even-tempered Gaussian fitting function[92],

$$V_{\mathrm{SR}}(r)=\sum_{k=0}^{7} a_k \exp\left(-\alpha\beta^k r^2\right) \tag{16}$$

The long-range term is a damped dispersion term based on Grimme's D3 formalism with the Becke–Johnson (BJ) damping function.[93,94]

$$V_{\mathrm{LR}}(r)=-\sum_{n=6,8} \frac{S_n C_n^{AB}}{r^n+\left(a_1 r_{AB}^0+a_2\right)^n} \tag{17}$$

where $r_{AB}^0=\sqrt{C_8^{AB}/C_6^{AB}}$, $S_6=1$, $S_8=2$, $a_1=0.5299$, $a_2=2.2$ Å, $C_6^{HH}=7.5916E_h a_0{}^6$, $C_8^{HH}=91.76991786E_h a_0{}^8$, $C_6^{OH}=10.8496E_h a_0{}^6$, $C_8^{OH}=169.45918093E_h a_0{}^8$. With V_{LR} given, the short-range sum is obtained by fitting $V_{\mathrm{PA}}-V_{\mathrm{LR}}$ as described below. To account for the spin-orbit effect, the short-range term in U_{22} is multiplied by a scaling factor of $(D_e - 140\mathrm{cm}^{-1})/D_e$, where D_e is the dissociation energy of the pairwise potential of OH in the original U_{22}. The scaling factor equals 0.9960924723525706. This value is chosen so that the nearly degenerate components of the $^2\Pi$ reactant have the correct splitting caused by the spin-orbit coupling.

The pairwise potential for OH* in the U_{33} diabatic potential energy surface, is written as two even-tempered Gaussian functions smoothly connected by a switching function,

$$V_{\mathrm{PA}}^{\mathrm{OH}^*}(r)=f_s(r)V_{\mathrm{SR}}^{\mathrm{OH}^*}(r)+\left[1-f_s(r)\right]V_{\mathrm{LR}}^{\mathrm{OH}^*}(r) \tag{18}$$

$V_{\mathrm{SR}}^{\mathrm{OH}^*}(r)$ has six terms, $V_{\mathrm{LR}}^{\mathrm{OH}^*}(r)$ has three terms, and the switching function is given by

$$f_s(r)=\frac{1}{2}\left[1-\tanh\left(\gamma\left(r-r_0\right)\right)\right] \tag{19}$$

with $\gamma=10$ Å^{-1} and $r_0=1.577$ Å.

For all three pairwise potentials (H_2, OH, and OH*), the linear coefficients a_k are determined by linear regression, and the non-linear parameters α and β are determined by nonlinear minimization using the constrained optimization by linear approximations algorithm[95] implemented on the *NLOpt* library.[96] The root-mean-square deviations (RMSDs) of the fitted pairwise potentials are 5×10^{-4} eV (30 points), 3×10^{-3} eV (56 points), and

2.6×10^{-2} eV (56 points) for H_2, OH, and OH*, respectively.

The many-body interaction in the diabatic potential energy surface fitting function is given by

$$V_{\mathrm{MB}} = \sum_{\substack{n_1+n_2+n_3+n_4+n_5+n_6=2, \\ \text{connected}}}^{M} D_{n_1 n_2 n_3 n_4 n_5 n_6} S\left[Y_1^{n_1} Y_2^{n_2} Y_3^{n_3} Y_4^{n_4} Y_5^{n_5} Y_6^{n_6} \right] \tag{20}$$

where $S\left[Y_1^{n_1} Y_2^{n_2} Y_3^{n_3} Y_4^{n_4} Y_5^{n_5} Y_6^{n_6} \right]$ are the symmetrized permutation-invariant polynomials[97,98] in mixed exponential-Gaussian (MEGs) variables[99],

$$Y_i\left(r_i\right) = \exp\left[-\frac{\left(r_i - r_{i,e}\right)}{a} - \frac{\left(r_i - r_{i,e}\right)^2}{b} \right] \tag{21}$$

The combination of eqs. (14) and (20) follows the approach[100] of adding pairwise terms to invariant polynomials obtained by monomial symmetrization[97,98] with the removal of disconnected terms[100] that can give spurious interactions in asymptotic regions.

For U_{11} and U_{22}, the nonlinear parameters of the MEG variables used in the present fit are $a = 0.8$ Å, $b = 1.0$ Å^2, $r_{i,e} = 1.2$ Å for HH distances and $a = 1.0$ Å, $b = 1.5$ Å^2, $r_{i,e} = 1.5$ Å for OH distances. For U_{33}, the nonlinear parameters of the MEG variables are $a = 0.8$ Å, $b = 1.0$ Å^2, $r_{i,e} = 1.2$ Å for HH distances and $a = 1.0$ Å, $b = 1.5$ Å^2, $r_{i,e} = 1.4$ Å for OH distances. The polynomial order of the fit is $M = 8$, leading to 545 independent coefficients $D_{n_1 n_2 n_3 n_4 n_5 n_6}$ that are determined by generalized least squares fitting using a weighting function on the square of the deviation given by

$$w_i = \begin{cases} 1 & \text{if} \quad \Delta U_i \le V_0 \\ \left(\dfrac{V_0}{\Delta U_i} \right)^2 & \text{if} \quad \Delta U_i > V_0 \end{cases} \tag{22}$$

where ΔU_i is the energy relative to H_2 + OH in the ground state and in their equilibrium geometries, and the threshold energy for decreasing the weights is $V_0 = 5.5$ eV. In addition,

the points near the ground-state reaction path are effectively weighted higher by replicating them in the data set.

The parameters of the potential energy surfaces are given in Fortran program that is included as a text file in the supplementary material.

IV.B. Diabatic Couplings. The diabatic couplings must be single-valued, which requires that they satisfy the following two conditions: (1) If we consider two indistinguishable geometries (i.e., geometries that differ only by permutation of identical particles, in this case that would be permutation of hydrogen atoms), $|U_{ij}|$ must be permutationally invariant. (2) We must be able to determine the sign of U_{ij} by assuming a particular symmetry under elementary transpositions and inversions. (Note that the adiabatic energies are independent of the sign of U_{12} when one has only two states, but they do depend on the signs of the couplings when one has three or more coupled states, as we have here.) Furthermore, the problem is nuanced by the fact that the adiabatic wave functions can have arbitrary signs as long as one is consistent. Consistency at a single geometry is trivial, but consistency of the signs from one geometry to another is trickier. In this subsection we discuss the practical scheme we developed for fitting the diabatic couplings to analytic functions satisfying these requirements. The problem of determining the signs of diabatic couplings is a general one (not restricted to the fourfold-way, but occurring in any diabatization scheme) – so the algorithm developed here may be more widely useful.

Although the adiabatic wave functions delivered by electronic structure programs and the diabatic wave functions delivered by the fourfold-way have arbitrary signs, the signs of diabatic matrix elements are only semi-arbitrary. To explain this, we first note that since **U** is symmetric and we are treating the case of three states, there are only three unique signs to consider, namely the signs of U_{12}, U_{13}, and U_{23}. Changing the sign of U_{12} corresponds to changing the sign of Φ_1 or Φ_2, but not both. Hence if we change the sign of U_{12}, we must also change the sign of U_{13} or U_{23}. For the present 3-state problem, we can summarize this requirement by saying that there must be an even number of sign changes of the three unique matrix elements, i.e., the product of the three sign changes must be +1.

IV.B.1. Cluster Growing Algorithm to Achieve Sign Consistency. As we have said, the signs of the diabatic couplings produced by the fourfold-way diabatization scheme are

arbitrary, and this arbitrariness adds a new dimension of difficulty to the fitting problem. For example, the diabatic couplings along an OH stretching path should be a smooth function of the OH internuclear distance; arbitrary phases can cause an oscillatory behavior and thereby degrade the accuracy of fitting. Here, we propose an algorithm called cluster growing to automatically achieve sign consistency. The idea of cluster growing algorithm is to start with an initial cluster of points where are confident of the sign assignments (for example, because none of the couplings passes through zero or close to zero in this region) and use this cluster to determine the phases of nearby points. The newly determined points are then added into the cluster, and another iteration is performed. At each iteration, the cluster grows.

At each iteration, the choice of "nearby" points is based on a distance criterion. The distances between the points are computed as the Euclidean distance in the six-dimensional internuclear-distance space of the OH_3 system. Figure 2(a) shows the pseudocode of the cluster growing algorithm. We start with an initial cluster, and for each point in the initial cluster, the nearby points are found based on a cutoff. Here, for each iteration, we use 0.001Å as an initial cutoff, and we increase this cutoff incrementally until we have at least 50 new points. Notice that a small cutoff increases the computational cost as well as the accuracy. Due to the large size of the data set, the cluster growing part is vectorized with graphics processing units (GPUs). The calculations were performed with Nvidia Tesla K40m GPUs installed on K40 GPU cluster of Minnesota Supercomputing Institute. Each K40m GPU has 2880 CUDA cores.

At the start of each iteration, the diabatic couplings of the points already in the cluster are fitted with permutationally invariant polynomials as discussed in detail in the next subsection. The total order of the permutationally invariant polynomials adaptively increases as the size of the cluster grows to achieve better accuracy of the fitting. The fit is used to predict the diabatic couplings of the new points and compare them with the computed values from the fourfold-way and model space diabatization. Based on the comparison, two signs are changed if a smaller difference of the values predicted values can be achieved with the even sign change product constraint. For example, computed and fitted diabatic couplings are 1.3 eV and -1.1 eV, the penalties of preserving and changing the phase are 2.4 eV and -0.2 eV, and hence a phase change would be preferred; but because all three diabatic couplings (U_{12},

U_{13} and U_{23}) are checked at once, the final decision on whether to change two signs is that we make the sum of the three penalties as small as possible. Figure 2(b) graphically shows the process of cluster growing. For the initial cluster of the iteration, as shown in the top panel, the diabatic couplings change smoothly from negative (red color) to positive (blue color) along a geometrical path. Such sign consistency is represented by the grey arrow. This initial cluster grows by finding the nearby points, but these new points do not necessarily have the correct signs as shown in the middle panel. The last panel shows the signs of new points after they are tailored by the algorithm such that a consistent sets of signs is achieved.

As an example, Fig. 3 shows the phase of the U_{13} changes before and after the cluster growing algorithm. Figure 3(a) introduces the labeling and the geometrical path. The O-H1 is fixed at 0.986 Å, and the H2-H3 distance is fixed at 0.800 Å. The center of the H2–H3 diatomic is labeled D. (Throughout the whole article, D always denotes either the center of H_B and H_C or the center of H2 and H3, depending on the context.) The angle of H2-O-H1 and the H3-O-H1 keeps the same and represented as the angle of D-O-H1. The two directions considered here are the O-H2 distance and the D-O-H1 angle. Figure 3(b) shows the U_{13} as a function of the two directions plotted in 1D. Within each grid, the O-H2 distances are the same and D-O-H1 angle changes from 90 to 180 degrees. One can see that U_{13} has different phase for a path with O-H_2 distance equals 1.1 Å (emphasized with light grey color) as compared with the other paths. Figures 3(c) and 3(d) show the dependence of U_{13} on the two coordinates as computed directly from the electronic structure theory and as tailored by the cluster growing algorithm. The portion with the wrong phase is emphasized by the light grey color in Fig. 3(c). The signed U_{13} is smooth after tailoring by the cluster growing algorithm. The achieved sign consistency of the diabatic couplings makes accurate analytical fitting possible.

IV.B.2. Symmetries of Diabatic Couplings, Choice of Analytical Functions, and Fitting. Diabatic wave functions do not necessarily satisfy point group symmetry. For example, valence bond functions are often reasonable choices for diabatic functions, but valence bond functions do not necessarily have point-group symmetry. We wish to take advantage of the nonuniqueness of diabatic representations to define our diabatic states to have certain symmetry properties – not point group symmetry but rather the molecular

symmetry group C_{2v}(M), where we use the notation of Bunker.[101] This group has is a subgroup of the D_{3h}(M) group, and it has three kinds of operations: identity, elementary transposition of two particles, and transposition–inversion, where we use the language of Rutherford.[102] All its irreducible representations are nondegenerate. Let A and B denote symmetry under elementary transposition P, and let 1 and 2 denote symmetry under P*, which is the combination of an elementary transposition and an inversion, so we have symmetries A_1, A_2, B_1, and B_2.[101,103] We emphasize that we are using irreducible representation labels here for symmetries in the molecular symmetry group C_{2v}(M) with operations P and P*, not for symmetries in C_{2v}. (When these symbols are used for C_{2v}, there is always a left superscript $2S+1$; thus $^2A_1$ is a C_{2v} label, whereas A_1 is a C_{2v}(M) label.) Table III shows the symmetry properties, where "A" and "1" denote even, and "B" and "2" denote odd. We want our diabatic state functions to transform as a definite irreducible representations of C_{2v}(M) because this will be very convenient for fitting the U_{jk} to functional forms for use in dynamics.. The diabatic couplings do not necessarily have A_1 symmetry, however, the product of the diabatic couplings, $U_{12}U_{13}U_{23}$, must transform as A_1.

Table IV provides analytic functions that transform according to the four irreducible representations, where **R** denotes the nuclear geometry, $c_m^{[jk]}$ is a linear coefficient to be determined by fitting, $\hat{T}_{AB}$ is an elementary transposition of hydrogen atom A with hydrogen atom B, $\hat{T}_{AB,AC}$ is a cyclic permutation obtained as AB followed by AC, $\mathbf{r}_{OA}$, $\mathbf{r}_{OB}$, and $\mathbf{r}_{OC}$ are vectors from oxygen to each of the three hydrogen atoms labeled as in Subsection III.B.1, and $P_m(\mathbf{R})$ is a monomial that is a product of exponentials of the magnitudes of the internuclear distances, and therefore $P_m(\mathbf{R})$ must be even under inversion. The inclusion of $\tanh\left[p\mathbf{r}_1\bullet(\mathbf{r}_2\times\mathbf{r}_3)\right]$ ensures the function is odd and smooth under the inversion operation, and p is a fitting parameter.. Note that $\left|\mathbf{r}_1\bullet(\mathbf{r}_2\times\mathbf{r}_3)\right|$ is equal to the volume of a parallelepiped with sides given by the three vectors; hence the magnitude of the argument of the $\tanh\left[p\mathbf{r}_{OA}\bullet(\mathbf{r}_{OB}\times\mathbf{r}_{OC})\right]$ function does not change under any permutation, but its sign changes under an elementary transposition as well as changing sign under an inversion.

By examining the behavior of the U_{jk} for paths that interchange the hydrogen atoms by inversion, by elementary transposition, or both, we found that U_{13} has A_1 symmetry, and U_{12} and U_{23} have B_1 symmetry.

The analytical function for fitting the A_1 coupling including permutational symmetry can be written as,

$$U_{jk}^{fit}(r_1,r_2,r_3,r_4,r_5,r_6) = \sum_{\substack{n_1+n_2+n_3+n_4+n_5+n_6=3, \\ \text{connected}}}^{M} D^{jk}_{n_1n_2n_3n_4n_5n_6} S\left(Y_1^{n_1}Y_2^{n_2}Y_3^{n_3}Y_4^{n_4}Y_5^{n_5}Y_6^{n_6}\right) \quad (23)$$

where $D^{jk}_{n_1n_2n_3n_4n_5n_6}$ is a coefficient determined by least-squares fitting, and the definitions of the other quantities are given above. Notice some important differences from functions used for the diabatic potential energy surfaces, namely that there is no constant term and no pairwise additive term, and the summation starts with the sum of the powers equal to three. In order to make the diabatic couplings vanish in the asymptote regions, all the disconnected terms are removed. The disconnected terms include all terms with the sum of the powers equal to 2 and some terms with the sum of the powers equal to 3. Hence, the total order starts with 3.

The U_{13} matrix element is directly fitted with a 12th order polynomial ($M = 12$) by using the A_1 function as shown in eq. (23). Although the MEG function of eq. (23) is defined in eq. (21), we use different a, b, and $r_{i,e}$ parameters for the fitting of U_{12}, U_{13}, and U_{23}. These parameters were optimized by fitting the diabatic couplings with various values of the parameters and fitting the mean unsigned deviations (MUDs) versus the values of parameters to a quadratic form to find optimized values. (We define unsigned deviation as the absolute magnitude of the difference between the value from the fit and the original electronic structure value.) The values used for the diabatic couplings are summarized in Table V, and the other parameters of the fits to the diabatic couplings are given in the Fortran program in the supplementary material. The MUD for the final fit to U_{13} is 0.097 eV.

The fittings of U_{12} and U_{23} are achieved by fits including only the nonplanar geometries since these functions vanish for planar geometries. In particular, we chose a value for p, and we fit $U_{jk}(\mathbf{R}) / \tanh\left[p\mathbf{r}_{OA}\cdot(\mathbf{r}_{OB}\times\mathbf{r}_{OC})\right]$ for nonplanar geometries to eq. (23). Notice $|\tanh x|$

is between 0 and 1, hence $\left|U_{jk}(\mathbf{R}) / \tanh\left[p\mathbf{r}_{OA}\cdot(\mathbf{r}_{OB}\times\mathbf{r}_{OC})\right]\right|$ is always larger than $\left|U_{jk}(\mathbf{R})\right|$. Figure S13 shows an example of mean unsigned deviation (MUD) as a function of p for U_{12} and U_{23}. (Figures with a prefix s are in Supplementary Material.) In this work, we use p = 15.4 Å^{-3} as the MUD is well converged with this value. Figure S14 shows the value of $\tanh\left[p\mathbf{r}_{OA}\cdot(\mathbf{r}_{OB}\times\mathbf{r}_{OC})\right]$ as a function of the signed volume $\left[\mathbf{r}_{OA}\cdot(\mathbf{r}_{OB}\times\mathbf{r}_{OC})\right]$ of a parallelepiped spanned by the three OH vectors with the currently selected p value. To further validate that the chosen p value can provide a smooth and odd function under the inversion operation, we have investigated how the diabatic couplings change under the inversion. Figure S15 shows how the diabatic couplings change along two paths that cross the planar geometry. Figures S15(a) and (c) show the geometries of the two paths, named the H-out-of-plane path and the H_2-out-of-plane path, corresponding to the motion of the H atom or H_2 molecule normal to the plane of original plane. For the H-out-of-plane path, the OH bond distances (O-H_A and O-H_B) of water are fixed at 0.966 Å and the H_AOH_B angle is fixed at 104.5 degrees, and at the planar geometry, the O-H_C distance is 2.304 Å. For the H_2-out-of-plane path, the O-H_A and H_B-H_C distances are fixed at 0.984 Å and 0.74 Å respectively, and at the planar geometry the distance between the O and the center of H_B and H_C is fixed at 2.00 Å. Figures S15(b) and (d) show the diabatic coupling in planes containing the two paths. One can see that fitted U_{12} and U_{23} are odd and smooth under the inversion motion, although the originally computed U_{12} and U_{23} were even because we employed the standard orientation. As we have removed the planar geometries from the database, to avoid over fitting, we fit U_{12} and U_{23} with a lower value of M, in particular with a 10th order polynomial (M = 10); we used MEG and Morse functions for U_{12} and U_{23} respectively. The MUDs for U_{12} and U_{23} are 0.087 and 0.069 eV respectively.

IV.B.3. Transformed adiabatic surfaces. The transformed adiabatic surfaces are obtained by diagonalizing the diabatic potential energy matrix at each nuclear configuration. The eigenvectors form the rotation matrix **T** between the adiabatic and diabatic wave functions. With the implemented analytical gradients for all 6 unique matrix elements (U_{11}, U_{22}, U_{33}, U_{12}, U_{13} and U_{23}), at nuclear geometry **R**, the analytical gradients of the adiabatic surfaces $\nabla_{\mathbf{R}}V_i$ and the nonadiabatic couplings $\mathbf{F}_{ij}$ between adiabatic states are computed

based on the following relations,[82]

$$\nabla_n V_i = \sum_{j,k} T_{ij}^* T_{ik} \nabla_{\mathbf{R}} U_{jk} \tag{24}$$

$$\mathbf{F}_{ij} = \begin{cases} \dfrac{1}{V_j - V_i} \sum_{k,l} T_{ik}^* T_{jl} \nabla_{\mathbf{R}} U_{kl} & (i \neq j) \\ \mathbf{0} & (i = j) \end{cases} \tag{25}$$

where T_{ij} has been introduced in eq. (5). Hence, the current coupled surfaces can be used in both adiabatic and diabatic representations.

V. ACCURACY OF THE CURRENT PES

In order to assess the quality of the fit, it is essential to specify the range over which it is intended to be used. In the key experiment of Todd et al.,[4] the OH is excited to V_3 with a photon of energy 4.0 eV. Adding the zero point energy of 0.4 eV and a possible thermal energy of 0.1 eV, gives 4.5 eV relative to the OH(r_e) + H_2(r_e) asymptote, where r_e is the equilibrium bond length. (Fu et al.[32] simulated the experiment with trajectories at 4.46 eV.) By considering all the geometries in the database with V_3 below 4.50 eV, the MUDs for V_1, V_2, and V_3 are 0.053, 0.031, and 0.077 eV respectively. This is a check of the fits of both the diabatic potentials and the diabatic couplings, since the transformed adiabats are obtained by diagonalizing the fitted DPEM.

In a fit it is important to ensure that the fitted potential remains high at higher-energy data points so the classically inaccessible regions on the accurate surfaces are also inaccessible on the fitted surfaces. By considering all the geometries in the database with V_3 below 7 eV, the MUDs for V_1, V_2, and V_3 are 0.075, 0.047 and 0.114 eV respectively.

We conclude that the fit is successful on average. Next we consider important geometries in more detail.

V.A. Ground and excited states of reactants and products. The ground-state equilibrium geometries for reactant and product are shown in Table VI. We compare to two previous fits to the ground-state surface[32,104] and to experiment.[105] Cuts through the ground-state PES corresponding to OH and HH stretching in the reactant region are shown in Fig. S16, and those corresponding to the three water vibrational modes are shown in Fig. S17.

These comparisons show that, although higher accuracy could be attained if one were fitting only the ground-state surface rather than three coupled surfaces, the current ground-state surface is accurate enough in the asymptotic regions for studies of nonadiabatic collisions.

The potential energy level of the product relative to the reactant is –0.70 eV, which compares well to our best estimate[106] of –0.71 eV.

V.B. van der Waals wells in reactant valley. We also investigated the geometry at the ground and excited state van der Waals (vdW) minima close to the reactant region. For this discussion, we consider five geometrical parameters, namely the O-H_A distance (R_{OH}), the H_B-H_C distance (R_{HH}), the distance between O and the center of H_BH_C (R_{OD}), the H_AOD angle (θ_1), and the ODH$_B$ angle (θ_2). We will compare these geometrical parameters from the current PES with those from SA-MCSCF/CI/pQZ calculations by Hoffman and Yarkony.[21] The results are shown in Table VII. Both the ground and excited states vdW minima show a T-shaped structure with H_A of the OH molecule pointed toward H_BH_C. (Notice these optimized structures are not exactly T-shaped (θ_1 = 0 deg and θ_2 = 90 deg), but they are very close to it.) For the ground-state vdW minimum, the fragment structures are very close to the optimized reactant structure, with O-D distance at 3.736 Å. For the excited state vdW minimum, the structure correctly shows a much smaller O-D distance at 2.219 Å with longer O-H_A and H_B-H_C bond lengths at 1.055 and 0.774 Å respectively. From the comparisons, one can see the current PES is acceptably accurate for the van der Waals minima.

V.C. Ground-state minimum-energy reaction path. Next we investigate the energy along an approximate minimum-energy path for the ground-state hydrogen transfer reaction. The comparisons between computed and fitted diabatic states and diabatic couplings along the MEP are shown in Figs. 4(a) and (b) respectively. Figure 4(c) shows the comparisons between the original and transformed adiabatic surfaces. Three representative geometries along the MEP corresponding to the reactant, transition state, and product regions are shown as inserts in Fig. 4(a). Figure 4 shows a clear crossing of the reactant and product diabatic states, similar to what is seen in a valence bond treatment[107] of the H + H_2 reaction; this behavior was expected from the electronic structure considerations summarized in Fig. 1. Although U_{11} and U_{33} cross along the MEP, the large value of the U_{13} coupling near the crossing geometries makes the V_1 and V_3 have a large separation all along the MEP.

Because the reaction path geometries are planar, U_{12} and U_{23} are zero along the reaction path, which is properly reflected in our fit. The MUDs of the transformed V_1, V_2, and V_3 along the reaction path (at a total of 31 geometries) are 0.053, 0.030, and 0.064 eV respectively. This confirms the accuracy of the fitted diabatic potentials and the fitted U_{13} along the reaction path.

V.D. From reactant to the tricoordinate region. The supplementary material presents results for two especially interesting two-dimensional cuts. Figure S1 corresponds to the H_2 rotational motion of Fig. 3(b) and is denoted as the HH rotation path; Figures S2, S3, and S4 are for an OH rotational motion illustrated in Fig. 5 of a previous publication[32] and is denoted as the OH rotation path. These figures show that the results for these geometries are accurate enough for realistic simulations.

V.E. Vibrational modes at transition state geometry. Figure 5 shows some cuts along the vibrational modes at the ground-electronic state saddle point for the chemical reaction. Representative geometries along the path are shown as inserts. We see most of transformed adiabatic surfaces agree very well with the originally computed ones. A large deviation is observed for V_3 in Fig. 5(d), however this region is at high energy (higher than 4.5 eV) and hence should have less relevance. Figures S18 and S19 show the fitted and computed diabatic states and diabatic couplings. The MUDs for transformed V_1, V_2, and V_3 for the four vibrational modes considered here (a total of 190 geometries) are 0.072, 0.022, and 0.119 eV. The transformed and computed V_1, V_2, and V_3 along the six normal modes computed from previous ground state adiabatic PES by Chen et al.[108] is shown in Fig. S20. Again, these accuracies are good enough for realistic simulations.

V.F. Vertical and adiabatic excitation energies of OH radical. The O-H distance at the optimized excited-state minimum of the reactant radical is 1.011 Å. At this excited-state minimum, the transformed adiabatic energy levels of the ground and excited states are 0.035 and 4.098 eV respectively (energies in this article are relative to $OH(r_e) + H_2(r_e)$). This indicates the classical-equilibrium-to-classical-equilibrium adiabatic excitation energy of the OH radical is 4.098 eV. Experiments yield a zero-point-level-to-zero-point-level adiabatic excitation energy of OH equal to 4.052 eV (32682.5 cm^{-1})[109], which is in reasonable agreement. The vertical excitation of the OH radical on our transformed adiabatic surfaces is

4.129 eV. By using the experimental adiabatic excitation energy of 4.052 eV) and the experimental fundamental vibrational frequency (3180.56 cm^{-1}) for the excited state, here we approximate the experimental vertical excitation energy should be 4.083 eV. Both comparisons show an energy difference of only 0.046 eV between the current PES and the corresponding experimental value.

V.G. PESs near conical intersections. An advantage of fitting the diabatic potential energy matrix elements is that the fitted surfaces should have qualitatively correct shapes near conical intersections. Unlike adiabatic PESs, the diabatic surfaces are smooth, and hence the fitting the PESs does not encounter additional difficulties near the conical intersections. In this subsection, we will report the comparisons between transformed and originally computed adiabatic surfaces at geometries near a conical intersection. A detailed analysis of conical intersection seams will be given in section VI.

The geometries considered in this regard are MRCI-optimized conical intersections reported in Refs. 21 and 37; because they are computed with MRCI, which is different from the XMC-QDPT method used here, they are not conical intersections of the present surfaces; however, the conical intersection geometries should be similar for the two treatments, and hence these geometries provide good test geometries for considering regions near a conical intersection. To enrich the diversity of our database, we have included our calculated results at these geometries in our fitting. We show in this subsection and in the supplementary information that the current PES is robust at these near-conical-intersection geometries.

The first near-conical-intersection geometry considered here is near a two-state intersection with C_{2v} symmetry (point #4 of Table III of Ref. 21); we will denote it as geometry P in the following text). The results near this conical intersection geometry are discussed in supplementary material in conjunction with Figures S7, S8, and S9.

Figure S21 shows two one-dimensional plots of the originally computed and transformed adiabatic surfaces as a function of the geometrical index for geometries in the branching plane of two C_{2v} and $C_{\infty v}$ conical intersection geometries. The C_{2v} conical intersection is the P geometry mentioned above and discussed in supplementary information, while the $C_{\infty v}$ conical intersection is a representative conical intersection with $C_{\infty v}$ symmetry (point #1 of Table IV in Ref. 21; the branching plane is discussed in the Ref. 36 as well).

These comparisons provide further confirmation that that current PES is accurate.

In addition, we have compared the energy levels of four high-symmetry points found to be minimal energy conical intersections (MECIs) within their symmetry at the MRCI theoretical level by Dillon and Yarkony[37]. The energy levels computed from the current PES and by XMC-QDPT are summarized in Table VIII. Again, we remind the reader that these geometries do not represent the MECIs on the XMC-QDPT PESs. For three of the four symmetries the XMC-QDPT and MRCI calculations agree well, with larger deviations for $C_{\infty v}$.

VI. ANALYSIS OF CURRENT PES

In this section, we will investigate the behavior of current PESs in various regions. Because this section only considers the fitted diabatic surfaces, fitted diabatic couplings, and transformed adiabatic surfaces, we will simply call them diabatic surfaces U_{ii}, diabatic couplings U_{ij}, and adiabatic surfaces V_i. We will order the following discussion from lower to higher symmetries. Specifically, we will investigate how the PESs change from nonplanar to planar geometries (C_s symmetry), how the PESs change along a path in C_s symmetry that connects the $C_{\infty v}$ and C_{2v} symmetries, and how the PESs change along coordinates that preserves C_{2v}, $C_{\infty v}$, C_{3v}, and D_{3h} symmetries.

The total number of nuclear internal degrees of freedom is denoted as F (which equals $3N-6$, where N is the number of atoms). For the present problem $F = 6$. The number of nuclear degrees of freedom for a subspace with a given symmetry is denoted as $\tilde{F}$ and is 5, 3, 3, 2, and 1 for C_s, C_{2v}, $C_{\infty v}$, C_{3v}, and D_{3h} symmetries, respectively. The dimension of a zero surface of the diabatic coupling in an $\tilde{F}$ -dimensional subspace is typically either 1 or $\tilde{F}$, where the latter implies that the diabatic coupling vanishes in the whole subspace due to an enforced symmetry. In the former case, the conical intersection seam has symmetry $\tilde{F}-2$; in the latter it has dimension $\tilde{F}-1$.

It is not required that diabatic wave functions transform according to an irrep of the relevant symmetry group, but in our analytic DPEM we do enforce some symmetries. If we enforced symmetry in all cases, we would find the following:

$$\begin{bmatrix} U_{11} & U_{12} & U_{13} \\ U_{12} & U_{22} & U_{23} \\ U_{13} & U_{23} & U_{33} \end{bmatrix} \rightarrow \begin{bmatrix} U_{11} & 0 & U_{13} \\ 0 & U_{22} & 0 \\ U_{13} & 0 & U_{33} \end{bmatrix} \rightarrow \begin{bmatrix} U_{11} & 0 & 0 \\ 0 & U_{22} & 0 \\ 0 & 0 & U_{33} \end{bmatrix} \quad (26)$$

C_1 C_s C_{2v} or $C_{\infty v}$

The behavior shown for C_s is built into our analytical functions. Therefore, diagonalizing the DPEM in C_s symmetry is equivalent to diagonalize a 2×2 matrix that involves U_{11}, U_{13}, and U_{33}. The resulting two transformed adiabatic states are $1^2A'$ and $2^2A'$ states; hence we label the conical intersection seam within C_s symmetry as the $2^2A'$-$1^2A'$ conical intersection. In the whole space this conical intersection has dimension $F - 2 = 4$; in the C_s space it has dimension $\tilde{F} - 2 = 3$; that is a three-dimensional subseam of the four-dimensional seam lies in C_s.

If one further changes the geometry from C_s symmetry to C_{2v} and $C_{\infty v}$ symmetries, eq. (26) shows all three diabatic couplings being zero; however, such symmetry is not present in our diabatization. Because all C_{2v} and $C_{\infty v}$ geometries are planar, we do have $U_{12} = U_{23} = 0$, but we do not force U_{13} to be zero for C_{2v} and $C_{\infty v}$ symmetries in the current fit. However, this has the consequence that our adiabatic states also have broken symmetry for these symmetries. The two states with A′ symmetry when OH_3 is in C_s symmetry become $1^2\Pi$ and $1^2\Sigma^+$ states when OH_3 in the $C_{\infty v}$ subspaces and 1^2B_2 and 1^2A_1 states when OH_3 in a C_{2v} subspace. Next we discuss the $1^2\Pi$-$^2\Sigma^+$ conical intersection seam and the diabatic crossing seam for $C_{\infty v}$ geometries and also the 1^2B_2-1^2A_1 conical intersection seam and the diabatic crossing seam for C_{2v} symmetries. The transformed surfaces corresponding to these two adiabatic states are obtained by diagonalizing a 2×2 matrix that contains U_{11}, U_{13}, and U_{33}. The two conditions for a conical intersection are $U_{11} = U_{33}$ and $U_{13} = 0$. Because we do not enforce $U_{13} = 0$, our fit has a conical intersection of dimensionality $\tilde{F} - 2 = 1$, but the dimensionality of the conical intersections in the C_{2v} and $C_{\infty v}$ subspaces should be $\tilde{F} - 1 = 2$. We alleviated this problem by including many C_{2v} and $C_{\infty v}$ geometries in our database in the hope of obtaining U_{13} as close to zero as possible. As a result, the fitted U_{13} are very close to zero, and conical intersection is approximately two-dimensional in these subspaces.

VI.A. From nonplanar to planar geometry. First we investigate how the PES changes

when one changes the OH_3 from nonplanar geometry to planar geometry. We start with a C_s geometry having O-H_A , H_B-H_C , and O-D distances of 1.0 Å, 1.2 Å, and 1.5 Å respectively, where O is at the origin, H_A has positive x coordinates, and D has negative x coordinate. Both H_A and D are on x-axis; H_B and H_C have positive and negative y-axis respectively, with H_B-D-O angle equals 60 degrees. In the following text, we will label this geometry as Q. We will investigate the following processes: (1) the H_BH_C out-of-plane motion that involves vertically moving H_BH_C out of the plane of the four atoms at geometry Q, (2) the motion that changes the O-D distance, and (3) the motion that changes the O-H_A distance.

The three adiabatic surfaces V_1, V_2, and V_3 are shown as a function of the out-of-plane coordinate of H_B-H_C, O-D distance, and O-H_A distance in Figs. 6(a), (c), and (e) respectively. The U_{11}, U_{22}, U_{33}, U_{12}, U_{13}, and U_{23} along the three coordinates are shown in Figs. 6(b), (d), and (f) respectively. Notice the geometries considered in Figs. 6(c), (d), (e), and (f) have C_s symmetry. Hence only U_{13} is shown in Figs. 6(c) and (e) because for planar geometries, U_{12} and U_{23} are exactly zero by symmetry. The adiabatic PESs and DPEM elements change smoothly for both in-plane and out-of-plane motions. One can see that U_{12} and U_{23} change sign smoothly when H_BH_C moves from one side of the plane formed at Q to the other side as shown in in Fig. 6(b). In addition, we find U_{11} and U_{22} has in general qualitatively similar behavior along different coordinates and are close in energy. Such behavior is consistent with that has been schematically illustrated for the global PESs as shown in Fig. 1.

An example of $2^2A'$ -$1^2A'$ conical intersection is shown in Fig. 6(c) where it is labeled as geometry Q1. At Q1, the O-D distance is 1.58 Å, and the rest of geometrical parameters are the same as for Q. The U_{11}, U_{22}, U_{33}, and U_{13} matrix elements are 2.400, 2.379, 2.415, and 0.003 eV respectively at Q1. The three transformed adiabatic surfaces are V_1 = 2.379, V_2 = 2.399, and V_3 = 2.415 eV at Q1. Notice that $V_1 = U_{22}$ at Q1 because U_{22} is decoupled from U_{11} and U_{33}. Hence, for the geometry Q1, the $2^2A'$ -$1^2A'$ conical intersection can be classified as a V_2-V_3 conical intersection. Figures S22(a) and (b) zoom into Figs. 6(c) and (d) in the range of O-D distance from 1.5 to 1.65 Å. These cuts clearly show the correct behavior of the PESs near the conical intersection. The cuspidal behavior at conical intersection cannot be achieved by a direct fit of the adiabatic surfaces, and hence this region of the surface shows the power of employing the DPEM as the fitting target. The PES along the O-H_A distance is

shown in Figs. 6(e) and (f).

Further discussing of the nonplanar-to-planar geometries is given in supplementary material.

VI.B. Connection among C_{2v}, , and $C_{\infty v}$ subspaces. Here we consider a motion that corresponds connections among C_{2v}, C_s, and $C_{\infty v}$ symmetries. The geometry labels are defined in Fig. 7(a), with O-H1 fixed at 1.0 Å. We are considering planar geometries with two coordinates corresponding to the H2H3 rotation around the center of H2H3, with the rotation angle changing from 0 to 90 degrees, and the H2-H3 distance changing from 0.6 to 1.4 Å. When the H2H3 rotation angle equals 0 and 90 degrees, the geometry has C_{2v} and $C_{\infty v}$ symmetry respectively. Hence, if one considers a change of the H2H3 rotation angle from 0 to 90 degrees, the path involves a $C_{\infty v}$ geometry changing to C_s and then to C_{2v} symmetry. The quantitiesU_{13}, U_{33} - U_{11}, and $V(2^2A')$ – $V(1^2A')$ (notice that at 0 degrees, the two states are $1^2\Pi$ and $1^2\Sigma^+$ states, while at 90 degrees, the two states are 1^2B_2 and 1^2A_1) are shown as functions of the H2H3 rotation angle and the H2-H3 distance in Figs. 7(b), (c), and (d) respectively. We can see from Fig. 7(b) that U_{13} is close to zero as a function of the H2-H3 distance for both $C_{\infty v}$ and C_{2v} geometries. One can see that $U_{33} - U_{11}$ changes from negative values for long H2-H3 distance and small rotation angle to positive values with short H2-H3 distance and large rotation angle. We have shown the two contour lines with values correspond to –0.335 eV and 0.523 eV in Fig. 7(c), and hence between these two contours, there must exist a diabatic crossing seam. This shows an example of how the diabatic crossing seam in C_s symmetry connects the diabatic crossing seams in $C_{\infty v}$ and C_{2v} symmetries. A $2^2A'$ -$1^2A'$ conical intersection seam can be found in Fig. 7(d), where it is shown as a black band with $2^2A'$ -$1^2A'$ below 0.2 eV. This gives an example of how such a $2^2A'$ -$1^2A'$ conical intersection seam in C_s symmetry connects a $1^2\Pi$-$1^2\Sigma^+$ conical intersection within the $C_{\infty v}$ subspaces to a 1^2B_2-1^2A_1 conical intersection within the C_{2v} subspace.

VI.C. Conical intersections and diabatic crossing seams in C_{2v} symmetry. Now we will discuss paths (cuts) that pass near (within about 0.2 eV) to the planar C_{2v} portions of the conical intersection seams and diabatic crossing seams. We consider 1^2B_2 and 1^2A_1 states for C_{2v} symmetry which corresponds to the transformed adiabatic surfaces by diagonalizing the 2×2 matrix involves U_{11}, U_{33} and U_{13}. We will show that in the current fit, U_{13} is very close

to zero for C_{2v} geometries, and 1^2B_2-1^2A_1 conical intersection seam and diabatic crossing seam form an approximately 2-dimensional surface in the 3-dimensional C_{2v} subspace.

Here we use O-H_A , H_B-H_C, and O-D distances as the coordinates in C_{2v} (recall from section IV.B.1 that in the present context D in as the center of the H_B-H_C diatomic). The geometries considered here are shown in Fig. 8(a), where the O-D distance is fixed at 1.5 Å. The U_{13}, $U_{33}-U_{11}$, and $|V(1^2B_2)-V(^2A_1)|$ contours are shown in Figs. 8(b), (c), and (d) respectively. In panels (b) and (c), the contours on either side of 0 are labeled. One can see that U_{13} is very close to zero for the geometries shown by the plots; it ranges from -0.09 to 0.08 eV. A diabatic crossing seam is found in the region where H_B-H_C is near 1.1 Å for shorter O-H_A distance and 1.3 to 1.4 Å for longer O-H_A distance, as can be seen from Fig. 8(b). Not surprisingly, due to the small values of U_{13}, conical intersection seam is located in a similar region. This can be observed from the black band as shown in Fig. 8(d).

We further consider two additional cuts corresponding to O-H_A fixed at 1.0 Å and H_B-H_C fixed at 1.2 Å. Figures 9(a), (b), and (c) show how $U_{33}-U_{11}$, U_{13}, and $|V(1^2B_2)-V(^2A_1)|$ change as functions of the O-D distance and H_B-H_C distance. One can observe a clear change from negative to positive for $U_{33}-U_{11}$ when the O-D distance increases. A diabatic crossing seam (green band in Fig. 9(a)) can be found for region where O-D is near 1.5 Å. The U_{13} matrix element is close to zero except for the region corresponding to an O-D distance around 1.0 Å and an H_B-H_C distance around 1.0 to 1.3 Å, with the largest U_{13} equal to 0.279 eV. We can see from Fig. 11(b) that U_{13} is close to zero as a function of the H2–H3 distance for both $C_{\infty v}$ and C_{2v} geometries at short H2–H3 distances. Therefore, one sees a conical intersection seam in Fig. 9(c) in the same region as the diabatic crossing seam, with the O-D distance near 1.5 Å. This conical intersection seam is shown as a thick black line in Fig. 9(c). Figure 9(d), (e), and (f) show how $U_{33}-U_{11}$, U_{13}, and $|V(1^2B_2)-V(^2A_1)|$ change as functions of the O-D distance and the O-H_A distance. Panels (d)–(f) are similar to panels (a)–(c) except that we fix H_A-H_B instead of O-H_A.

The geometries with $|U_{33}-U_{11}| < 0.2$ eV and $|V(1^2B_2)-V(^2A_1)| < 0.2$ eV are plotted in Fig. 10 as a 3-dimensional scatter plot as a function of the O-H_A , H_B-H_C, and O-D distances with the O-H_A distance in the range 0.9 to 1.4 Å, the H_B-H_C distance in the range 0.6 to 1.4 Å, and the O-D from 1.0 to 3.0 Å with a step size of 0.05 Å. Panels (a) and (b) show scatter plots

with two different perspectives, with black dots represent the geometries with $|U_{33}\text{-}U_{11}| < 0.2$ eV and the red dots representing geometries with $|V(1^2B_2) - V(^2A_1)| < 0.2$ eV. The yellow surface shown in the figure represents the 2-dimensional surface of the diabatic crossing and conical intersection seam in the 3-dimensional space. One can see that most of the geometries indicated in the scatter plot are on both diabatic crossing and conical intersection seam (with black and red color on the same dot). This illustrates our previous analysis that the diabatic crossing and conical intersection seam will be both 2-dimensional. In addition, panels (c) and (d) show the distribution of U_{13} for geometries satisfying the 0.2 eV criteria. We see that U_{13} is very close to zero for these geometries.

VI.D. Conical intersections and diabatic crossing seams in $C_{\infty v}$ symmetry. In this section, we consider the $1^2\Pi\text{-}^2\Sigma^+$ conical intersection seam and diabatic crossing seam in the $C_{\infty v}$ subspace. Based on the previous discussion, we know that the conical intersection and diabatic crossing seams are 2-dimensioanl in $C_{\infty v}$. In this section, we will show that U_{13} is fitted close to zero.

We use the three O-H distances as representative coordinates, as shown in Fig. 11(a). Figures 11 (b), (c), and (d) shows the U_{13}, $U_{33} - U_{11}$, and $|V(1^2\Pi) - V(1^2\Sigma^+)|$ as functions of the O-H2 and O-H3 distances with the O-H1 distance at 1.0 Å. In addition, we are considering the situation where OH3 is at least 0.5 Å longer than OH2 to avoid a strong H2-H3 repulsive potential. Figure 11(b) shows that U_{13} ranges from -0.10 to 0.10 eV, with most of the region close to zero, indicated by the green color. One can observe a green band in Fig. 11(c) near the diagonal of the of the coordinate space considered here. A contour line marked with 0.044 eV shows that the diabatic crossing seam is located nearby. A black band shown in Fig. 11(d) indicates the location of the conical intersection seam, which is close to the region where the diabatic states cross. Figure 12 shows a similar scenario for the $C_{\infty v}$ subspace with O-H2 at 1.5 Å and changing the O-H1 distance from 0.9 to 1.4 Å and the O-H3 distances from 2.0 to 4.0 Å.

Similar to the procedure we employed for C_{2v} subspace, Fig. 13 shows an analysis of the conical intersection seam in the region with O-H1 from 0.9 to 1.4 Å, O-H2 from 0.9 to 1.9 Å, and O-H3 from 1.4 to 4.4 Å with the O-H3 distance at least 0.5 Å bigger than the O-H2 distance. We again used a step size of 0.05 Å. Black and red dots indicate the geometries with

less than 0.2 eV for $|U_{33}-U_{11}|$ and $|V(1^2\Pi) - V(1^2\Sigma^+)|$ respectively. One can see that black and red dots are almost on top of each other, as they should be.

VI.E. D_{3h} region and a path from D_{3h} to C_{3v}. In the D_{3h} subspace, we only have one independent degree of freedom, namely the O-H distance. Figure 14(a) shows the three adiabatic surfaces as a function of OH distance ranging from 0.9 to 1.5 Å. The V_1, V_2, and V_3 surfaces are shown as red, blue, and yellow curves respectively; due to the degeneracy between V_2 and V_3, blue and yellow curves are on top of each other. Such degeneracy is required by D_{3h} symmetry. The two nearly degenerate states have single occupancies of one or another of the two 2*e* SOMOs shown as DMO7 and DMO9 in Table I. The dominant DSFs for the associated states U_{11} and U_{22} are χ_1 and χ_5 respectively. Although we don't enforce the D_{3h} symmetry in the construction of diabatic states, Fig. 14(a) shows the current fit is very accurate in the D_{3h} subspace in that the two adiabatic states are nearly degenerate. Figure 14(b) shows the U_{11}, U_{22}, U_{33}, and U_{13} of the corresponding region in D_{3h} symmetry. The fitted U_{11} and U_{22} preserves such degeneracy for D_{3h} configurations.

Now we start with each geometry in D_{3h} symmetry considered in Fig. 14, and we consider the out-of-plane motion of the three H atoms to see how the PESs behave when one changes from D_{3h} to C_{3v}. At the D_{3h} configuration, the four atoms are in the *xy*-plane, and we change the symmetry from D_{3h} region to C_{3v} region by moving the O atom vertically in the *z* direction between -1.0 and 1.0 Å. The adiabatic surfaces V_1, V_2, and V_3 as functions of the O-H distance and out-of-plane coordinate are shown in Figs. 15(a), (b), and (c) respectively. It is shown that V_2 and V_3 are nearly degenerate (notice the color bars are the same for Figs. 15 (b) and (c)), which indicates the current fit is robust for C_{3v} symmetries.

VI.F. Diabatic state crossing along a reaction path. Here we consider the diabatic state crossings along a reaction path. This path involves the O-H2 and O-H3 distances changing with a fixed O-H1 distance of 0.962 Å and a fixed D-O-H1 angle of 103.7 degrees. The H1, H2, and H3 labels are defined in Fig. 16(a), and D is the center of H2 and H3. Notice O, H2, and H3 are collinear with O-H3 at least 0.6 Å longer than O-H2. We are considering the O-H2 distance from 0.8 to 2.6 Å and the O-H2 distance from 1.4 to 3.2 Å. Figure 16(b) shows the diabatic state ordering along the path. The U_{11}-U_{22} diabatic state crossing is also shown in Fig. 16(c). Figures 16(d) and (e) show the U_{11}-U_{33} and U_{22}-U_{33} diabatic state

crossings. One can see that Figs. 16(d) and (e) are very similar. Along the path, U_{33} crosses both U_{11} and U_{22} once. This is consistent with what has been illustrated in schematic Fig. 1. The reaction of H_2 with OH to form H_2O + H can be approximately understood by following a path starting from the upper right corner of Fig. 16(b) and following the diagonal boundary to a shorter O-H2 distance, then vertically going up to a longer O-H3 distance. Along such a path, one would observe U_{33} cross both U_{11} and U_{22} one time and the system maintain the $U_{33} < U_{22} < U_{11}$ diabatic state ordering. Figure S23 is a similar figure with the D-O-H1 angle at 120 degrees.

VI.G. Nonadiabatic coupling vectors. We consider an example of the NACs as a function the H_BH_C out-of-plane motion described in section VI.A. The transformed adiabatic states and DPEM elements along the H_BH_C out-of-plane motion are shown in Fig. 6(a) and (b). The magnitudes of the NACs between the three transformed adiabatic states, $|\boldsymbol{F}_{12}|$, $|\boldsymbol{F}_{13}|$, and $|\boldsymbol{F}_{23}|$, are shown in Fig. 17. One can see $|\boldsymbol{F}_{13}|$ and $|\boldsymbol{F}_{23}|$ are much larger than $|\boldsymbol{F}_{12}|$ along the path. This can be understood from Fig. 6(b), which shows that along the H_BH_C out-of-plane motion, U_{11} and U_{22} cross with U_{33}, and U_{13} and U_{23} deviate significantly from zero. One also sees that $|\boldsymbol{F}_{12}|$ can be small even though the energy gap between the transformed adiabatic states V_1 and V_2 is small, for example, where the H_BH_C out-of-plane coordinate ranges from -1.0 to 0.5 Å. This is because the two states are weakly coupled, and Fig. 6(b) shows that U_{12} is close to zero along the path.

VII. CONCLUSION

We have performed three-state XMC-QDPT calculations for more than 70000 geometries to explore the global coupled potential energy surfaces of the OH_3 system and to develop analytic fits that can be used for investigating the quenching reactions of excited hydroxyl radical with H_2. The diabatic states and diabatic couplings are obtained by employing the fourfold-way and model space diabatization at each geometry. Each matrix element in the diabatic matrix (U_{11}, U_{22}, U_{33}, U_{12}, U_{13} and U_{23}) is fitted with a suitable analytical function that takes account of the invariance with respect to permuting the H atoms, and a new algorithm is used for determining the phases of the off-diagonal diabatic matrix elements. The adiabatic surfaces are subsequently obtained by diagonalizing the

diabatic potential energy matrix at each nuclear geometry; the adiabatic energies obtained in this way from the fits are called the transformed adiabatic energies. With the implemented analytical derivative of diabatic states and diabatic couplings, the gradients of the adiabatic surfaces and nonadiabatic couplings can also be computed.

By comparing the originally computed adiabatic energies and the transformed adiabatic energies, the mean unsigned deviations of V_1, V_2, and V_3 are 0.053, 0.031, and 0.077 eV respectively for geometries with V_3 below 4.5 eV. In addition, we have compared the transformed adiabatic energies to the originally computed XMC-QDPT adiabatic surfaces along various cuts and at some critical geometries, for example near conical intersections and at ground-state and excited-state van der Waals minima. These comparisons show high accuracy for the analytic fit. Due to the smoothness of the diabatic states and diabatic couplings, the current fit can correctly predict the PESs near the conical intersection geometries.

Further analysis investigated various regions of the PESs in greater detail. Specifically, we have shown how the PESs behave when one changes the OH_3 molecule from nonplanar to planar geometry, when one changes the OH_3 molecule within the C_s symmetry along a path that connects the $C_{\infty v}$ and C_{2v} symmetries, and when one changes the molecule along paths that preserve C_{2v}, $C_{\infty v}$, C_{3v}, and D_{3h} symmetries. We have also mapped out the 1^2B_2-1^2A_1 conical intersection seam and diabatic crossing seam within the C_{2v} symmetry, the $1^2\Pi$-$^2\Sigma^+$ conical intersection seam and diabatic crossing seams within the $C_{\infty v}$ symmetry, and diabatic crossing s among U_{11}, U_{22}, and U_{33} along an approximate reaction path. These results have shown the current PES is reasonably accurate near conical intersections. Hence, we believe the current fit can be employed to investigate the dynamical behaviors of the quenching reactions of excited hydroxyl radical with H_2.

POTENTIAL ENERGY MATRIX: SURFACES AND COUPLINGS

Fortran subroutines containing the fits to the potential energy surfaces and couplings are included in the supplementary material. These files can also be obtained from the Potlib library at https://comp.chem.umn.edu/potlib. A manual for the PES subroutines is also included in the supplementary material.

SUPPLEMENTARY MATERIAL

See supplementary material for Fortran routines containing the fitted surfaces and additional figures containing mean unsigned deviations, the hyperbolic tangent inversion function, diabatic potential energy matrix elements, and adiabatic potential energy surfaces.

ACKNOWLEDGMENTS

The authors are grateful to Steven Mielke (deceased, Dec. 28, 2017) for contributions to preliminary stages of the research, and the authors are grateful to Hua Guo, Ahren Jasper, Eugene Kamarchik, Marsha Lester, David Yarkony, and Donghui Zhang for stimulating interactions. This work was supported in part by the U.S. Department of Energy, Office of Science, Office of Basic Energy Sciences under Award Number DE-SC0015997. A.G.S.de O.-F. acknowledges support from the Coordenação de Aperfeiçoamento de Pessoal de Nível Superior - Brasil (CAPES) - Finance Code 001 and the Conselho Nacional de Desenvolvimento Científico e Tecnológico (CNPq) under grants 306830.

Table I. Point-group symmetries of the DMOs

DMO	Character in OH + H_2 region[a]	Local symmetry[a]		Character in tricoordinate region	Local symmetry		Character in H_2O + H region[b]	Local symmetry[b]	
		C_s	C_{2v}		C_s	C_{2v}		C_s	C_{2v}
1	$2s$	a'	a_1	$2s$	a'	a_1	$2s$	a'	a_1
2	σOH_A	a'	a_1	$1e_{p_{x,y}}$	a'	b_2	$1b_2H_2O$	a'	b_2
3	$2p_yO$	a'	b_2	$1e_{p_{x,y}}$	a'	a_1	$2a_1H_2O$	a'	a_1
4	$2p_zO$	a''	b_1	$1b_1$	a''	b_1	$2p_zH_2O$(HOMO)	a''	b_1
5	σH_BH_C	a'	a_1	$\sigma^*OH_A + \sigma^*OH_B + \sigma^*OH_C$	a'	a_1	$1s$H	a'	a_1
6	$3p_yO$	a'	b_2	$3e$	a'	a_1	$a_1 / 3p$	a'	a_1
7	$3d_{z^2}O$	a'	a_1	$2e$	a'	b_2	$3d_{xy}$	a'	b_2
8	$3p_xO/\sigma^*OH_A$	a'	a_1	$3e$	a'	b_2	$\sigma^*OH_A + \sigma^*OH_B$	a'	b_2
9	$\sigma^*H_BH_C$	a'	b_2	$2e$	a'	a_1	$3s / 4a_1H_2O$(LUMO)	a'	a_1
10	$3p_zO$	a''	b_1	$3p_zO$	a''	b_1	$3p_zO$	a''	b_1
11	$3sO$	a'	a_1	$3sO$	a'	a_1	$6a_1$	a'	a_1

[a] For OH + H_2 we define the symmetry as follows for this table: all four atoms lie in the xy plane, the O atom is at the origin, the x-axis coincides with the OH bond, and HH is orthogonal to OH forming a T-shape structure

[b] For H_2O + H we define the symmetry as follows for this table: H_2O is in the xy plane, the O atom is at the origin, the x-axis is on the HOH bisector, and the separated H is on this bisector axis.

Table II. Orbital occupancies[a] and point-group symmetries[b] of prototype configurations of the diabatic states

State	DSF	Occupancies[b]	Local symmetry[a]		
			Reactants	Tricoordinate	Products
1	χ_1	2222 00100	$^2A_1$	$^2B_2$	$^2B_2$
1	χ_2	2212 20000	$^2B_2$	$^2A_1$	$^2A_1$
1	χ_3	2221 10001,S	$^2A_2$	$^2B_1$	$^2B_1$
2	χ_4	2221 20000	$^2B_1$	$^2B_1$	$^2B_1$
2	χ_5	2222 00001	$^2B_2$	$^2A_1$	$^2A_1$
2	χ_6	2221 10001,T	$^2A_2$	$^2B_1$	$^2B_1$
3	χ_7	2122 20000	$^2A_1$	$^2B_2$	$^2B_2$
3	χ_8	2222 10000	$^2A_1$	$^2A_1$	$^2A_1$

[a] The local symmetry elements for reactant-like and product-like regions are defined in Table I. The tricoordinate column is for D_{3h} structures, but classified according to the symmetry in the C_{2v} subgroup so that one can see how the states evolve when the symmetry is broken in dynamics. Symmetry information is presented here only to characterize the states; symmetry is not imposed in actual calculations.

[b] These are the occupancies of the first nine DMOs of Table I; DMOs 10 and 11have zero occupancy in all of the prototype configurations. S and T denote the spin coupling by denoting whether the state dissociates to singlet water or triplet water in the product region.

Table III. Symmetry properties[a] of the C_{2v}(M) group

irrep	Identity	Transposition (P)	Inversion (*)	Transposition-Inversion (P*)
A_1	even	even	even	even
A_2	even	even	odd	odd
B_1	even	odd	odd	even
B_2	even	odd	even	odd

[a]adapted from Serre (ref.103)

Table IV. Symmetry-adapted functions for the C_{2v}(M) group

irrep	Function
A_1	$U_{jk}(\mathbf{R}) = \sum_m c_m^{[jk]}(1+\hat{T}_{AB}+\hat{T}_{BC}+\hat{T}_{AC}+\hat{T}_{AB,AC}+\hat{T}_{AB,BC})P_m(\mathbf{R})$
A_2	$U_{jk}(\mathbf{R}) = \tanh\left[p\mathbf{r}_{OA}\bullet(\mathbf{r}_{OB}\times\mathbf{r}_{OC})\right]\sum_m c_m^{[jk]}(1-\hat{T}_{AB}-\hat{T}_{BC}-\hat{T}_{AC}+\hat{T}_{AB,AC}+\hat{T}_{AB,BC})P_m(\mathbf{R})$
B_1	$U_{jk}(\mathbf{R}) = \tanh\left[p\mathbf{r}_{OA}\bullet(\mathbf{r}_{OB}\times\mathbf{r}_{OC})\right]\sum_m c_m^{[jk]}(1+\hat{T}_{AB}+\hat{T}_{BC}+\hat{T}_{AC}+\hat{T}_{AB,AC}+\hat{T}_{AB,BC})P_m(\mathbf{R})$
B_2	$U_{jk}(\mathbf{R}) = \sum_m c_m^{[jk]}(1-\hat{T}_{AB}-\hat{T}_{BC}-\hat{T}_{AC}+\hat{T}_{AB,AC}+\hat{T}_{AB,BC})P_m(\mathbf{R})$

Table V. The MEG parameters used for fitting diabatic coupling

Diabatic Couplings	a / Å		b / Å^2		$r_{i,e}$ / Å	
	HH	OH	HH	OH	HH	OH
U_{12}	0.800	0.610	1.300	1.300	0.702	0.802
U_{13}	1.1028022	1.2561573	1.61	1.75	0.9333333	1.196078
U_{23}	1.09	1.323343	1.633190	1.823343	1.001178	1.113545

Table VI. The equilibrium geometries, harmonic vibrational frequencies, and energies of the optimized ground state minima at reactant and product regions

	Property[a]	Present PES	FKB[b]	YZCL[c]	Ref.
OH	r_e	0.972	0.967	0.97	0.970 [d]
	ω	3759	3737	3764	3738 [d]
H_2	r_e	0.745	0.740	0.742	0.741 [d]
	ω	4378	4401	4406	4401 [d]
H_2O	r_e	0.965	0.962	0.959	0.959 [d]
	θ_e	103.7	103.8	104.2	104.3 [d]
	ω_1	3694	3788	3859	3825 [d]
	ω_2	1809	1653	1649	1654 [d]
	ω_3	3850	3879	3961	3936 [d]
$OH+H_2 \rightarrow H_2O+H$[f]	ΔV_1[f]	-0.70	-0.64	-0.68	-0.71[g]

[a] Bond lengths (r) are in Å, bond angles (θ) are in degrees, vibrational frequencies are in cm^{-1}, energy of reaction is in eV. The vibrational frequencies are ω_1 for the symmetric stretch, ω_2 for the bend, and ω_3 for the asymmetric stretch.

[b] Fu, Kamarchik, and Bowman, fir to MRCISD+Q/aug-cc-pVTZ calculations, Ref. 32

[c] Yang, Zhang, Collins, and Lee, fit to a mixture of QCISD(T)/ 6-311++G(3df,2pd), IC-MRCISD+Q/aug-cc-pVTZ, and UCCSD(T)/aug-cc-pVQZ calculations, Ref. 102

[d] Experiment, Refs. 103 and 107

[f] Energy of $H_2O(r_e, \theta_e)$ + H relative to $OH(r_e) + H_2(r_e)$

[g] Best estimate, Ref. 104

Table VII. The geometries and energies of the optimized ground and excited state van der Waals minima close to the reactant region.

PESs	this work		DY[a]	
State	$OH(X^2\Pi)$ $+H_2(X^1\Sigma_g^+)$	$OH(A^2\Sigma^+)$ $+H_2(X^1\Sigma_g^+)$	$OH(X^2\Pi)$ $+H_2(X^1\Sigma_g^+)$	$OH(A^2\Sigma^+)$ $+H_2(X^1\Sigma_g^+)$
R_{OH} / Å	0.970	1.055	0.977	1.059
R_{HH} / Å	0.743	0.774	0.744	0.778
R_{OD} / Å	3.736	2.219	3.310	2.175
θ_1 / deg	6.25	1.36	0.55	0.04
θ_2 / deg	90.52	89.08	90.42	89.92
D_e (eV)	0.039	0.375	0.027	0.312
$V - V^*$/eV[b]	-3.805	0.000	-3.860	0.000

[a] Dillon and Yarkony, SA-MCSCF/CI Ref. 21.

[b] To compare with Ref. 21, we provide the energy relative to V^*, which is the energy of the excited-state van der Waals minimum of the corresponding PES.

Table VIII. The energy levels of four high-symmetry minimal energy conical intersections optimized at MRCI method[a], all energies are relative to the $OH\left(A^2\Sigma^+\right)+H_2\left(X^1\Sigma_g^+\right)$ state at the reactant geometry.

States	C_{2v} / eV	$C_{\infty v}$ / eV	C_{3v} / eV	D_{3h} / eV
		Current PES[b]		
V_1	2.612	2.066	0.408	0.593
V_2	2.771	2.291	2.590	2.628
V_3	2.957	2.317	2.644	2.690
		XMC-QDPT calculation		
V_1	2.626	2.087	0.374	0.592
V_2	2.772	2.281	2.570	2.680
V_3	2.826	2.281	2.570	2.680
		MRCI calculation[c]		
V_1	2.622	2.265	0.421	0.654
V_2	2.870	2.265	2.613	2.722
V_3	2.870	2.265	2.613	2.722

[a]Notice that these geometries are not optimized high-symmetry minimal energy conical intersections at XMC-QDPT method, a clear discrepancy can be seen from the results between XMC-QDPT and MRCI calculations

[b]Energy relative to the $OH\left(X^2\Pi\right)+H_2\left(X^1\Sigma_g^+\right)$ state at OH(r_e)+H2(r_e) in eV, the reference energy is -76.8015361068575E_h.

[c]Ref. 37.

Figure captions

Fig. 1. Diabatic states and their dominant configurations at the reactant, tricoordinate, and product regions. The orbitals are labeled in standard orientation and their characters are given in Table I. The vertical direction is potential energy (but only in a schematic sense, not in a quantitative way), and horizontal direction is a schematic reaction coordinate that passes through the three regions. The solid curves represent the diabatic states, and dotted curves represent the diabatic prototype states.

Fig. 2. (a) Pseudocode of the cluster growing algorithm. (b) The top, middle, and bottom panels are graphical representations of the phases of the initial cluster of the iteration, the cluster growing intermediate, and the final cluster of the iteration. The color bar from red to blue indicates the values of diabatic couplings changes from more negative side to more positive side. The grey arrow in top and bottom panels represent the phase consistency, where the arrow points from the direction of negative to positive values of the diabatic coupling under consideration.

Fig. 3 (a) The definition of labels and the two directions considered. (b) A comparison of computed and fitted U_{13} as a function of the two directions plotted in 1D. Within each segment (segments are separated by thin vertical lines in the plot), the O-H2 distance is constant and D-O-H1 angle changes from 90 to 180 degrees, where D in the figure is the center of the H2-H3 fragment. Then the O–H2 distance is increased for the next segment. The original matrix elements produced with the wrong phases are shown in a red on a grey background. (c) and (d) two-dimensional plot of computed and fitted U_{13}, respectively, as functions of the two directions. The grey color highlights the part with wrong signs in part c.

Fig. 4 (a) Comparisons between computed and fitted (a) diabatic states and (b) diabatic couplings along the reaction path. (c) Comparisons between computed and transformed adiabatic surfaces along MEP. The inserted pictures in (a) are representative geometries along the MEP; oxygen and hydrogen atoms are shown with red and white colors respectively. The reaction path starts at a geometry in the reactant region (where the equilibrium values of the geometric parameters are O-H_A = 0.969 Å, O-H_B = 2.049 Å, $\angle H_A OH_B = 94.47°$, H_C-H_B=0.743 Å), proceeds to the transition state region (where the geometry of the transition structure has O-H_A = 0.968 Å, O-H_B = 1.343 Å, $\angle H_A OH_B = 98.70°$, and H_C-H_B = 0.814 Å), and finally goes to the product region (where the equilibrium structure of the product has O-H_A = 0.954 Å, O-H_B = 0.956 Å, $\angle H_A OH_B = 105.21°$, and O-$H_C$ = 2.630 Å).

Fig. 5. Comparisons between computed and transformed adiabatic surfaces along vibrational modes at the transition state geometry. The inserted pictures indicate representative geometries along the paths.

Fig. 6. (a), (b) The adiabatic surfaces (V_1, V_2, and V_3) and the DPEM elements (U_{11}, U_{22}, U_{33}, U_{12}, U_{13}, and U_{23}) along the out-of-plane coordinate of H_BH_C. (c), (d) The adiabatic surfaces (V_1, V_2, and V_3) and DPEM elements (U_{11}, U_{22}, U_{33}, and U_{13}) as functions of the O-D distance. (e), (f) The adiabatic surfaces (V_1, V_2, and V_3) and DPEM elements (U_{11}, U_{22}, U_{33}, and U_{13}) as functions of the O-H_A distance.

Fig. 7. (a) Illustration of the H2H3 rotation angle and the H1, H2, H3 labeling. The figure shows U_{13}, U_{33}-U_{11}, and $V(2^2A') - V(1^2A')$ as functions of the H2H3 rotation angle and the H2-H3 distance in (b), (c), and (d) respectively. Notice in (d) that at 0 degrees, the two states are $1^2\Pi$ and $1^2\Sigma^+$ states, while at 90 degrees, the two states are 1^2B_2 and 1^2A_1 states

Fig. 8. (a) Notation used in this figure, corresponding to C_{2v} symmetry with the O-D distance fixed at 1.5 Å. (Note that D is the center of the H_A–H_B diatomic.) (b) U_{13}, (c) $U_{11} - U_{33}$, and (d) $|1^2B_2$-$1^2A_1|$ as functions of the O-H_A and H_B-H_C distances.

Fig. 9. Contour maps as functions of the O–D distance and another distance, where D is the center of H_B–H_C. (a) U_{11}-U_{33}, (b) U_{13}, and (c) $|1^2B_2$-$1^2A_1|$ for a two-dimensional cut with the O-H_A distance fixed at 1.0 Å, where the O-D distance changes from 1.0 to 3.0 Å, and the H_A-H_B changes distance from 0.6 to 1.4 Å. (d) U_{11}-U_{33}, (e) U_{13}, and (f) $|1^2B_2$-$1^2A_1|$ for a two-dimensional cut with the H_A-H_B distance fixed at 1.2 Å, where the O-D distance changes from 1.0 to 3.0 Å, and the O-H_A distance changes from 0.9 to 1.4 Å.

Fig. 10. Conical intersection and diabatic crossing seams shown as a scatter plot in the 3-dimensional space of O-H_A , H_B-H_C, and O-D distances. The black and red dots represent geometries with $|U_{33}$-$U_{11}| < 0.2$ eV and $|1^2B_2$-$1^2A_1| < 0.2$ eV respectively. A 2-dimensional surface with yellow color represents the conical intersection and diabatic crossing seam in the C_{2v} symmetry subspace. These two seams are shown with (a) top-down and (b) bottom-up perspectives. The distribution of U_{13} for the geometries with $|1^2B_2$-$1^2A_1| < 0.2$ eV and $|U_{33}$-$U_{11}| < 0.2$ eV are shown in (c) and (d) respectively.

Fig. 11. (a) Notation used in this figure, corresponding to $C_{\infty v}$ symmetry with the O-H1 distance fixed at 1.0 Å. (b) U_{13}, (c) U_{33}-U_{11}, and (d) $|1^2\Pi$-$1^2\Sigma^+|$ as functions of the O-H2 and O-H3 distances.

Fig. 12. (a) U_{11}-U_{33}, (b) U_{13}, and (c) $|V(1^2\Pi) - V(1^2\Sigma^+)|$ for a two-dimensional cut with the O-H2 distance fixed at 1.5 Å, where the O-H1 distance changes from 0.9 to 1.4 Å, and the O-H3 distance changes from 2.0 to 4.0 Å. (d) U_{11}-U_{33}, (e) U_{13}, and (f) $|1^2\Pi$-$1^2\Sigma^+|$ for a two-dimensional cut with the O-H3 distance fixed at 2.5 Å, where the O-H1 distance changes from 0.9 to 1.4 Å, and the OH2 distance changes from 0.9 to 1.9 Å.

Fig. 13. Conical intersection and diabatic crossing seams shown as a scatter plot in the 3-dimensional space of O-H1, O-H2, and O-H3 distances. The black and red dots represent geometries with $|U_{33}-U_{11}| < 0.2$ eV and $|1^2\Pi-1^2\Sigma^+| < 0.2$ eV respectively. A 2-dimensional surface with yellow color represents the conical intersection and diabatic crossing seam in the C_{2v} symmetry subspace. These two seams are shown with (a) top down and (b) bottom up perspectives. The distribution of U_{13} for the geometries with $|1^2\Pi-1^2\Sigma^+| < 0.2$ eV and $|U_{33}-U_{11}| < 0.2$ eV are shown in (c) and (d) respectively.

Fig. 14. (a) V_1, V_2, and V_3, (b) U_{11}, U_{22}, U_{33}, and U_{13} as functions of the O-H distance for D_{3h} symmetry. In panel (a), the yellow and blue curves are on top of each other. In panel (b), the red and blue curves are on top of each other.

Fig. 15. (a) V_1, (b) V_2, and (c) V_3 as functions of O-H distance and out-of-plane coordinate for C_{3v} symmetry

Fig. 16. (a) The labeling of H1, H2, and H3. (b) Diabatic state orders along the O-H2 and O-H3 distances. The U_{11}-U_{22}, U_{11}-U_{33}, and U_{22}-U_{33} diabatic state crossings are shown in (c), (d) and (e) respectively.

Fig. 17. The magnitudes $|\boldsymbol{F}_{12}|$, $|\boldsymbol{F}_{13}|$, and $|\boldsymbol{F}_{23}|$ of the nonadiabatic coupling vectors in units of $Å^{-1}$ as functions of the H_BH_C out-of-plane motion.

References

[1] R. A. Loomis and M. I. Lester, Annu. Rev. Phys. Chem. **48**, 463 (1997).
[2] M. I. Lester, R. A. Loomis, R. L. Schwartz, and S. P. Walch, J. Phys. Chem. A **101**, 9195 (1997).
[3] D. T. Anderson, M. W. Todd, and M. I. Lester, J. Chem. Phys. **110**, 11117 (1999).
[4] M. W. Todd, D. T. Anderson, and M. I. Lester, J. Phys. Chem. A **105**, 10031 (2001).
[5] D. R. Crosley, in *Progress and Problems in Atmospheric Chemistry*, Advanced Series in Physical Chemistry – Vol. 3, edited by J.R. Barker (World Scientific, Singapore,1995), pp. 256-317.
[6] B. L. Hemming, D. R. Crosley, J. E. Harrington, and V. Sick, J. Chem. Phys. **115**, 3099 (2001).
[7] B. L. Hemming and D. R. Crosley, J. Phys. Chem. A **106**, 8992 (2002).
[8] D. E. Heard and D. A. Henderson, Phys. Chem. Chem. Phys. **2**, 67 (2000).
[9] J. Luque and D. R. Crosley, *LIFBASE: Database and Spectral Simulation Program* (Version 1.6), SRI Int. Rep. MP 99-009 (SRI Int., Menlo Park, CA, 1999).
[10] R. P. Wayne, *Chemistry of Atmospheres*, 3rd ed. (Oxford Univ. Press, New York, 2000).
[11] A. Fiore, Nature **513**, 176 (2014).
[12] I. Glassman and R. Yetter, *Combustion*, 4th ed. (Academic, Boston, 2008).
[13] J. H. Lehman and M. I. Lester, Annu. Rev. Phys. Chem. **65**, 537 (2014).
[14] D. R. Yarkony, *Rev. Mod. Phys*. **68**, 985 (1996).
[15] D. G. Truhlar and C. A. Mead, Phys. Rev. A **68,** 32501 (2003).
[16] B. G. Levine and T. J. Martinéz. Annu. Rev. Phys. Chem. **58**, 613 (2007).
[17] S. Matsika and P. Krause, Annu. Rev. Phys. Chem. **62**, 621 (2011).
[18] W. Domcke and D. R. Yarkony, Annu. Rev. Phys. Chem. **63**, 325 (2012).

[19] Y. Shu, B. S. Fales, W.-T. Peng, and B. G. Levine, J. Phys. Chem. Lett. **8**, 4091 (2017).
[20] B. G. Levine, M. P. Esch, B. S. Fales, D. T. Hardwick, W.-T. Peng, and Y. Shu, Annu. Rev. Phys. Chem. **70**, 21 (2019).
[21] B. C. Hoffman and D. R. Yarkony, J Chem. Phys. **113**, 10091 (2000).
[22] C. A. Mead, J. Chem. Phys. **70**, 2276 (1979).
[23] S. Matsika and D. R. Yarkony, J. Chem. Phys. **115**, 5066 (2001).
[24] M. Ortiz-Suárez, M. F. Witinski, and H. F. Davis, J. Chem. Phys. **124**, 201106 (2006).
[25] I. B. Pollack, Y. Lei, T. A. Stephenson, and M. I. Lester, Chem. Phys. Lett. **421**, 324 (2006).
[26] P. A. Cleary, L. P. Dempsey, C. Murray, M. I. Lester, J. Kłos, and M. Alexander, J. Chem. Phys. **126**, 204316 (2007).
[27] L. P. Dempsey, C. Murray, P. A. Cleary, and M. I. Lester, Phys. Chem. Chem. Phys. **10**, 1424 (2008).
[28] P. Dempsey, C. Murray, and M. I. Lester, J. Chem. Phys. **127**, 151101 (2007).
[29] M. D. Wheeler, D. T. Anderson, M. W. Todd, M. I. Lester, P. J. Krause, and D. C. Clary, Mol. Phys. **97**, 151 (1999).
[30] M. D. Wheeler, D. T. Anderson, and M. I. Lester, Int. Rev. Phys. Chem. **19**, 501 (2000).
[31] E. Kamarchik, B. Fu, and J. M. Bowman, J. Chem. Phys. **132**, 091102 (2010).
[32] B. Fu, E. Kamarchik, and J. M. Bowman, J. Chem. Phys. **133**, 164306 (2010).
[33] J. H. Lehman, L. P. Dempsey, M. I. Lester, B. Fu, E. Kamarchik, and J. M. Bowman, J. Chem. Phys. **133**, 164307 (2010).
[34] R. Conte, B. Fu, E. Kamarchik, and J. M. Bowman, J. Chem. Phys. **139**, 044104 (2013).
[35] P.-Y. Zhang, R.-F. Lu, T.-S. Chu, and K.-L. Han, J. Phys. Chem. A **114**, 6565 (2010).
[36] P.-Y. Zhang, R.-F. Lu, T.-S. Chu, and K.-L. Han, J. Chem. Phys. **133**, 174316 (2010).
[37] J. Dillon and D. R. Yarkony, J. Phys. Chem. A **117**, 7344 (2013).
[38] J. Dillon and D. R. Yarkony, J. Chem. Phys. **139**, 064314 (2013).
[39] M. A. Collins, O. Godsi, S. Liu, and D. H. Zhang, J. Chem. Phys. **135**, 234307 (2011).
[40] Q. Ma, J. Kłos, M. H. Alexander, A. van der Avoird, and P. J. Dagdigian, J. Chem. Phys. **141**, 174309 (2014).
[41] C. A. Mead and D. G. Truhlar, Chem. Phys. **277**, 31 (2002).
[42] A. W. Jasper, B. K. Kendrick, C. A. Mead, and D. G. Truhlar, in *Modern Trends in Chemical Reaction Dynamics: Experiment and Theory (Part 1)*, Advanced Series in Physical Chemistry – Vol. 14, edited by X. Yang and K. Liu (World Scientific, Singapore, 2004), pp. 329-391.
[43] M. S. Child, in *Atom-Molecule Collision Theory*, edited by R. B. Bernstein (Plenum, New York, 1979), pp. 427-465.
[44] S. Chapman, Adv. Chem. Phys. **82**, 423 (1992).
[45] R. Valero and D. G. Truhlar, J. Chem. Phys. **125**, 194305 (2006).
[46] J. M. Bowman, G. Czakó, and B. Fu, Phys. Chem. Chem. Phys. **13**, 8094 (2011).
[47] M. J. T. Jordan, K. C. Thompson, and M. A. Collins, J. Chem. Phys. **102**, 5647 (1995)
[48] K. C. Thompson, M. J. T. Jordan, and M. A. Collins, J. Chem. Phys. **108**, 8302 (1998)
[49] R. P. Bettens and M. A. Collins, J. Chem. Phys. **111**, 816 (1999).
[50] O. Tishchenko and D. G. Truhlar, J. Chem. Phys. **130**, 024105 (2009)
[51] F. Spiegelmann and J. P. Malrieu, J. Phys. B **17**, 1259 (1984).
[52] R. Cimiraglia, J.-P. Malrieu, M. Persico, and F. Spiegelmann, J. Phys, B **18**, 3073 (1985).
[53] H.-J. Werner, B. Follmeg, and M. H. Alexander, J. Chem. Phys. **89**, 3139 (1988).
[54] T. Pacher, L. S. Cederbaum, and H. Köppel, J. Chem. Phys. **89**, 7367 (1988).
[55] P. Halvick and D. G. Truhlar, J. Chem. Phys. **96**, 2895 (1992).
[56] K. Ruedenberg and G. J. Atchity, J. Chem. Phys. **99**, 3799 (1993).
[57] G. J. Atchity and K. Ruedenberg, Theor. Chem. Acc. **97**, 47 (1997).
[58] R. G. Sadygov and D. R. Yarkony, J. Chem. Phys. **109**, 20 (1998)
[59] E. S. Kryachko and D. R. Yarkony, Int. J. Quantum Chem. **76**, 235 (2000).
[60] H. Nakamura and D. G. Truhlar, J. Chem. Phys. **115**, 10353 (2001).

[61] R. Abrol and A. Kuppermann, J. Chem. Phys. **116**, 1035 (2002).
[62] M. P. Fülscher and L. Serrano-Andrés, Mol. Phys. **100**, 903 (2002).
[63] H. Nakamura and D. G. Truhlar, J. Chem. Phys. **117**, 5576 (2002).
[64] H. Nakamura and D. G. Truhlar, J. Chem. Phys. **118**, 6816 (2003).
[65] O. Godsi, C. R. Evenhuis, and M. A. Collins. J. Chem. Phys. **125**, 104105 (2006).
[66] B. N Papas, M. S. Schuurman, and D. R. Yarkony, J. Chem. Phys. **129**, 124104 (2008).
[67] K. R. Yang, X. Xu, and D. G. Truhlar, Chem. Phys. Lett. **573**, 84 (2013).
[68] C. E. Hoyer, X. Xu, D. Ma, L. Gargliardi, and D. G. Truhlar, J. Chem. Phys. **141**, 114104 (2014).
[69] X. Zhu and D. R. Yarkony, J. Chem. Phys. **140**, 024112 (2014).
[70] X. Zhu and D. R. Yarkony J. Phys. Chem. A **119**, 12383 (2015).
[71] C. E. Hoyer, K. A. Parker, L. Gargliardi, and D. G. Truhlar, J. Chem. Phys. **144**, 194101 (2016).
[72] D. M. G. Williams and W. Eisfeld, J. Chem. Phys. **149**, 204106 (2018).
[73] Z. Varga, K. A. Parker, and D. G. Truhlar, Phys. Chem. Chem. Phys. **20**, 26643 (2018).
[74] R. Valero and D. G. Truhlar, J. Chem. Phys. **125**, 194305 (2006).
[75] S. Nangia and D. G. Truhlar, J. Chem. Phys. **124**, 124309 (2006).
[76] Z. Li, R. Valero, and D. G. Truhlar, Theor. Chem. Acc. **118**, 9 (2007).
[77] X. Xu, K. R. Yang, and D. G. Truhlar, J. Chem. Theory Comp. 9, 3612 (2013).
[78] X. Xu, J. Zheng, K. R. Yang, and D. G. Truhlar, J. Amer. Chem. Soc. **136**, 16378 (2014).
[79] K. R. Yang, X. Xu, J. Zheng, and D. G. Truhlar, Chem. Sci. **5**, 4661 (2014).
[80] S. L. Li, and D. G. Truhlar, J. Chem. Phys. **146**, 064301 (2017).
[81] L. Zhang, D. G. Truhlar, and S. Sun Phys. Chem. Chem. Phys. **20**, 28144 (2018).
[82] A. W. Jasper and D. G. Truhlar, in *Conical Intersections: Theory, Computation, and Experiment*, edited by W. Domcke, D. R. Yarkony, and H. Köppel (World Scientific, Singapore, 2011), pp. 375-412.
[83] H. Nakano, J. Chem. Phys. 99, 7983 (1993).
[84] H. Nakano, Chem. Phys. Lett. **207**, 372 (1993).
[85] H. Nakano, T. Nakajima, T. Tsuneda, and K. Hirao, J. Mol. Struct. **573**, 91 (2001).
[86] A. A. Granovsky, J. Chem. Phys. **134**, 214113 (2011).
[87] K. Ruedenberg, L. M. Cheung, and S. T. Elbert, Int. J. Quantum Chem. **16**, 1069 (1979).
[88] T. H. Dunning, Jr. J. Chem. Phys. **90**, 1007 (1989).
[89] O. Tishchenko, J. Zheng, and D. G. Truhlar, J. Chem Theory Comput. **4**, 1208 (2008).
[90] H.A. Witek, Y.-K. Choe, J.P. Finley, and K. Hirao, J. Comput. Chem. **10**, 957 (2002).
[91] S. L. Li, and D. G. Truhlar, J. Chem. Phys. **142**, 064106 (2015).
[92] L. Bytautas, N. Matsunaga, and K. Ruedenberg, J. Chem. Phys. **132**, 074307 (2010).
[93] S. Grimme, S. Ehrlich, and L. Goerigk, J. Comput. Chem. **32**, 1456 (2011).
[94] S. Grimme, J. Antony, S. Ehrlich, and H. Krieg, J. Chem. Phys. **132**, 154104 (2010), 0405167.
[95] M. J. D. Powell, Acta Numer. **7**, 287 (1998).
[96] S. G. Johnson, *The NLopt nonlinear-optimization package*, http://ab-initio.mit.edu/nlopt
[97] B. J. Braams and J. M. Bowman, Int. Rev. Phys. Chem. **28**, 577−606 (2009).
[98] Z. Xie and J. M. Bowman, J. Chem. Theory Comput. **6**, 26−34 (2010).
[99] J. D. Bender, P. Valentini, I. Nompelis, Y. Paukku, Z. Varga, D. G. Truhlar, T. Schwartzentruber, and G. V. Candler, J. Chem. Phys. **143**, 054304 (2015).
[100] Y. Paukku, K. R. Yang, Z. Varga, and D. G. Truhlar, J. Chem. Phys. **139**, 044309 (2013), **140**, 019903(E) (2014).
[101] P. R. Bunker, *Molecular Symmetry and Spectroscopy* (Academic Press, New York, 1979)
[102] D. E. Rutherford, *Substitutional Analysis* (Hafner, New York, 1968).
[103] J. Serre, Adv. Quantum Chem. **8**, 1 (1974).
[104] M. Yang, D. H. Zhang, M. A. Collins, and S.-Y. Lee, J. Chem. Phys. **115**, 174 (2001).

[105] G. Herzberg, *Molecular Spectra and Molecular Structure. IV. Constants of Diatomic Molecules* (Krieger, Malabar, 1979).
[106] Y. Wang, P. Verma, X. Jin, D. G. Truhlar, and X. He, Proc. Natl. Acad. Sci. USA **115**, 10257 (2018).
[107] I. Yasumori, Bull. Chem. Soc. Japan **32**, 1110 (1959).
[108] J. Chen, X. Xu, X. Xu, and D. H. Zhang, J. Chem Phys. **138**, 154301 (2013).
[109] G. Herzberg, *Molecular Spectra and Molecular Structure. I. Spectra of Diatomic Molecules* (Van Nostrand Reinhold, New York, 1950).